

Performance Benchmarks for 2-View and 3-View Fiber-Projection Fine-Grained Particle Detectors

Haohui Che^a and Guang Yang ^{†,b,1}

^a*Washington University in St. Louis, St. Louis, MO 63130, USA*

^b*Brookhaven National Laboratory, Upton, NY 11973, USA*

E-mail: [†] gyang1@bnl.gov

ABSTRACT: Fine-grained scintillator detectors are critical for precision measurements in nuclear and particle physics, where accurate reconstruction of interaction vertices and secondary particle directions enables separation of signal from background events. A well-known design choice is the fiber readout geometry: traditional 2-View systems use orthogonal X and Y fibers, while next-generation 3-View designs add a third Z-fiber layer that provides unambiguous 3D voxel identification. The 2-View approach suffers from combinatorial ghost hits, that the false 3D candidates arising from fiber projection ambiguities, degrading reconstruction performance in high-multiplicity events. This paper presents comprehensive simulation benchmarks quantifying the performance difference between 2-View and 3-View geometries across key metrics. We find that the 3-View geometry reduces ghost hits by 30–90% depending on event topology, provides robust vertex resolution across complex topologies, and maintains superior angular resolution for shower direction reconstruction. These benchmarks inform the design optimization of future detectors and provide quantitative guidance for reconstruction algorithm development across a broad range of experiments including neutrino physics, rare kaon/pion decays, and collider calorimetry.

KEYWORDS: Scintillators, 3D-projection readout, Neutrino Detectors, Collider Calorimeter, Particle Tracking Calorimeter

¹Corresponding author.

Contents

1	Introduction	1
1.1	Physics Motivation	1
1.2	3-View Detector Concept	2
1.3	Ghost Hit Problem	2
1.4	Paper Purpose and Structure	3
2	Simulation Framework	3
2.1	Detector Model	3
2.2	Optical Simulation Assumptions	4
2.3	Electronics and Noise Considerations	4
2.4	Particle Generation and Geometry	4
2.5	Fiber Readout denotation	6
2.6	Reconstruction Algorithms	6
3	Ghost Hit Suppression	6
3.1	Analytical Demonstration	6
3.1.1	Definitions	7
3.1.2	Ghost Formation in 2-View Geometry	7
3.1.3	Ghost Suppression in 3-View Geometry	8
3.1.4	Case 1: Track-Like Topology (Line) with (θ, ϕ) Dependence	9
3.1.5	Case 2: Shower-Like Topology (Cone)	11
3.1.6	Summary of Scaling Laws	14
3.2	Quantitative Comparison	14
3.3	Orientation Dependence (θ, ϕ)	15
4	Single-Shower Angular Resolution	17
4.1	Angular Resolution (θ, ϕ) Dependence	18
5	Single-Shower Vertex Resolution	19
5.1	Vertex Finding Algorithm	19
5.2	Vertex Resolution (θ, ϕ) Dependence	21
6	Two-Shower Vertex Resolution	22
6.1	Two-Shower Vertex Finding Algorithm	22
6.2	Results	23
7	Energy-Dependent Performance for Particles through Matter	25
7.1	Energy vs Angular Resolution at Three Orientations	26
7.2	Angular Resolution Heatmaps at Fixed Energies	30
8	Conclusion	32

A Fine Pitch Studies (0.5 cm)	35
A.1 Scaling Expectations	35
A.2 Angular Resolution vs Cone Opening	35
A.3 Angular Resolution Heatmaps	36
A.4 Ghost Hit Heatmaps	37
A.5 Single-Track Vertex Resolution	39
A.6 Vertex Resolution Heatmaps	39
A.7 Energy-Dependent Performance	41
A.8 Summary and Scaling Validation	44

1 Introduction

Fine-grained scintillator detectors have become essential tools across multiple frontiers of nuclear and particle physics. Their combination of tracking capability and calorimetric response makes them particularly suitable for experiments requiring precise reconstruction of complex final states. This paper presents comprehensive simulation benchmarks comparing two fundamental readout geometries: the traditional 2-View and the next-generation 3-View approach. We quantify the performance gains in ghost hit suppression, angular resolution, vertex resolution, and energy-dependent particle reconstruction.

1.1 Physics Motivation

The demand for fine-grained 3D hit reconstruction spans a remarkably diverse range of physics programs. Firstly, neutrino oscillation experiments such as the ongoing T2K [1], NOvA [2] experiments, require near detectors that precisely reconstruct the interaction vertex and identify outgoing particle multiplicities to constrain neutrino-nucleus cross sections [3]. The T2K Fine-Grained Detectors demonstrated few-centimeter vertex resolution [4], and the upgraded SuperFGD extends this with 3-View readout [5, 6]. Future experiments including DUNE [7–9] and Hyper-Kamiokande [10] are considering similar concepts. In addition, experiments searching for rare kaon decays such as NA62 ($K^+ \rightarrow \pi^+ \nu \bar{\nu}$) [11, 12] and KOTO ($K_L \rightarrow \pi^0 \nu \bar{\nu}$) [13] require hermetic photon vetoes to reject backgrounds from $\pi^0 \rightarrow \gamma \gamma$. The PIONEER experiment [14, 15] probes lepton universality through precision $\pi^+ \rightarrow e^+ \nu$ measurements, demanding excellent tracking in the decay region. Furthermore, Particle Flow Calorimetry at future $e^+ e^-$ colliders (ILC, CLIC, FCC-ee) requires unprecedented spatial granularity to separate nearby showers [16]. The CMS HGCAL [17] and EIC detectors [18, 19] also employ highly granular scintillator sampling sections. Additionally, fine-grained scintillators also find use in dark matter veto systems, muon tomography, medical beam monitoring, and cosmic ray physics. A systematic understanding of the advantage of the 3D-projection readout over the 2D-projection readout through optical fiber is beneficial to the future particle detector design and optimization.

1.2 3-View Detector Concept

The fundamental architecture of a 3-View (3V) scintillator detector is illustrated in Figure 1. The active volume consists of an array of optically isolated scintillator cubes (voxels), each penetrated by three orthogonal wavelength-shifting (WLS) fibers running along the X, Y, and Z directions. When a charged particle traverses a cube and deposits energy via ionization, scintillation light is produced isotropically within the cube. A fraction of this light is captured by each of the three WLS fibers, wavelength-shifted, and guided to Multi-Pixel Photon Counters (MPPCs) located at the fiber ends.

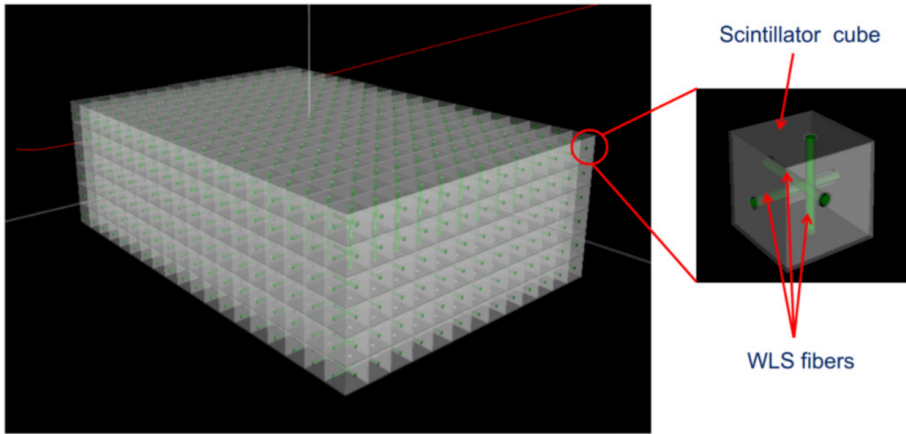


Figure 1: The 3-View scintillator detector concept. Each cubic voxel is read out by three orthogonal wavelength-shifting fibers (X, Y, Z), with MPPCs at the fiber ends. The highlighted cube illustrates the triple-fiber readout geometry. Figure is taken from [20].

In a traditional 2-View (2V) geometry, only X and Y fibers are employed. A hit at position (x, y, z) lights the X-fiber passing through (y, z) and the Y-fiber passing through (x, z) . Reconstruction identifies candidate hit positions by finding all combinations where both an X-fiber and a Y-fiber are lit at the same z -layer.

1.3 Ghost Hit Problem

The 2-View geometry suffers from a fundamental combinatorial ambiguity. Consider two true hits at positions (x_1, y_1, z) and (x_2, y_2, z) in the same z -layer. The detector records four lit fibers: X-fibers at (y_1, z) and (y_2, z) , and Y-fibers at (x_1, z) and (x_2, z) . The reconstruction algorithm evaluates all fiber crossings, yielding four candidates: the two true hits (x_1, y_1) and (x_2, y_2) , plus two “ghost” candidates (x_1, y_2) and (x_2, y_1) that do not correspond to real energy deposits.

In general, N true hits in a single z -layer produce N^2 candidates, of which only N are genuine and $N^2 - N$ are ghosts. This quadratic scaling creates severe problems in high-multiplicity events. **Ghost contamination:** Ghost contamination degrades vertex resolution by biasing the reconstructed position toward ghost centroids and corrupts angular reconstruction by introducing spurious hit directions. Furthermore, it inflates apparent energy deposits, biasing calorimetric measurements, and complicates pattern recognition by creating false track and shower candidates.

The 3-View geometry introduces a third constraint through the Z-fiber. A true hit at (x, y, z) now lights three fibers: X-fiber at (y, z) , Y-fiber at (x, z) , and Z-fiber at (x, y) . A candidate hit is accepted only if *all three* corresponding fibers register signals.

For the example above with two true hits, the Z-fibers lit are only those at (x_1, y_1) and (x_2, y_2) . The ghost candidates at (x_1, y_2) and (x_2, y_1) fail the Z-fiber requirement and are rejected. The 3-View geometry thus provides natural ghost suppression through topological constraints, without requiring energy matching or timing information.

However, the 3-View geometry does not eliminate *all* ghosts. Certain symmetric hit configurations, such as four hits arranged on a rectangular prism, create fiber coincidences that satisfy the triple constraint at ghost positions as well. These irreducible ghost hits represent a fundamental limit of the light-projection-based approach.

1.4 Paper Purpose and Structure

Despite the conceptual clarity of the 3-View advantage, quantitative benchmarks are essential for detector optimization. This work addresses several key questions such as the ghost reduction factor as a function of event topology and hit multiplicity, 3-View improvement on angular resolution for shower direction reconstruction, vertex resolution gain that achieved for single and multi-shower events, and the improvement scaling with particle energy and scintillator granularity. This paper addresses these questions through comprehensive Monte Carlo simulation, providing quantitative guidance for detector design decisions. The results are applicable to a broad range of experiments employing fine-grained scintillator technology.

The paper is organized as follows. Section 2 describes the simulation framework, including the detector model, particle generation, optical assumptions, and reconstruction algorithms. Section 3 quantifies ghost hit suppression across different event topologies, from track-like to shower-like configurations, and presents analytical derivations of the expected ghost counts. Section 4 evaluates single-shower angular resolution as a function of shower parameters and particle direction. Section 5 and 6 present vertex resolution studies for both single-shower and two-shower topologies. Section 7 examines energy-dependent performance for realistic muon and electron simulations spanning 100 MeV to 10 GeV. Finally, Section 8 summarizes key findings and discusses implications for future detector designs. Appendix A replicates all studies at finer pitch (0.5 cm) to demonstrate performance scaling.

2 Simulation Framework

2.1 Detector Model

We model a generic fine-grained scintillator detector as a cubic voxelized volume with baseline pitch $p = 1.0$ cm. The detector spans approximately 1 m^3 in the simulation, though results and conclusions are largely independent of detector size for the topologies studied. All main results use the 1.0 cm baseline. Appendix A presents a complete replication of all studies at finer pitch ($p = 0.5$ cm) to validate performance scaling and demonstrate that further improvements are achievable with even smaller voxel sizes.

2.2 Optical Simulation Assumptions

In this study, we employ an idealized optical model where scintillation light is perfectly confined within each cube-shaped voxel and is collected only by the three orthogonal wavelength-shifting (WLS) fibers penetrating that voxel. This perfect confinement approximation does not account for optical crosstalk, where the leakage of scintillation photons through the fiber holes into neighboring cubes.

Measurements with physical prototypes of the SuperFGD detector [5, 6] have characterized this optical crosstalk. Light leakage through the ~ 1 mm diameter fiber holes was measured to be approximately 3% per face, with total crosstalk to nearest-neighbor cubes estimated at 5–10% depending on the reflective coating quality. This crosstalk can either be treated as a systematic effect that degrades resolution, or with appropriate calibration, that can be exploited as additional position information to improve hit localization beyond the voxel pitch limit.

The perfect confinement assumption in our simulation therefore represents a conservative scenario. In practice, crosstalk signals provide sub-voxel position information that can enhance angular and vertex resolution. Future simulations incorporating crosstalk modeling are expected to show modest improvements beyond the results presented here, particularly at coarser pitch values where the crosstalk fraction relative to the primary signal is smaller.

2.3 Electronics and Noise Considerations

Our simulation assumes noiseless hit detection, with which a voxel is marked as “lit” if and only if a charged particle trajectory passes through it. We do not include any thermal noise, dark count rates of the Multi-Pixel Photon Counters (MPPCs/SiPMs), or readout electronics noise.

This idealization is justified for several reasons. Modern MPPCs achieve dark count rates of order 10^5 – 10^6 Hz at room temperature [21], which corresponds to $\lesssim 0.1\%$ occupancy per voxel in a 100 ns readout window, which is negligible compared to the signal hit densities considered in this study. The SuperFGD detector employs customized MPPCs with photon detection efficiency $>25\%$ and crosstalk probability $<3\%$ [22]. Combined with front-end ASICs providing thresholds of 0.5–1 photoelectron equivalent, the false hit rate from electronics noise is suppressed to levels that do not significantly impact reconstruction.

Furthermore, the ghost hit phenomenon under study is a combinatorial effect arising from fiber projection ambiguities, not from noise hits. The addition of a small random noise floor would increase the total candidate count slightly but would not qualitatively change the 2-View vs. 3-View comparison, as noise affects both geometries equally.

For these reasons, we expect our noiseless assumption to accurately represent the physics of ghost hit formation and the relative performance gains of 3-View readout. Quantitative predictions for specific detector implementations should incorporate realistic noise models calibrated to prototype measurements.

2.4 Particle Generation and Geometry

The simulation generates particles with controlled geometric parameters to systematically explore the reconstruction phase space. Figure 2 illustrates the key parameters for single-cluster and two-cluster topologies.

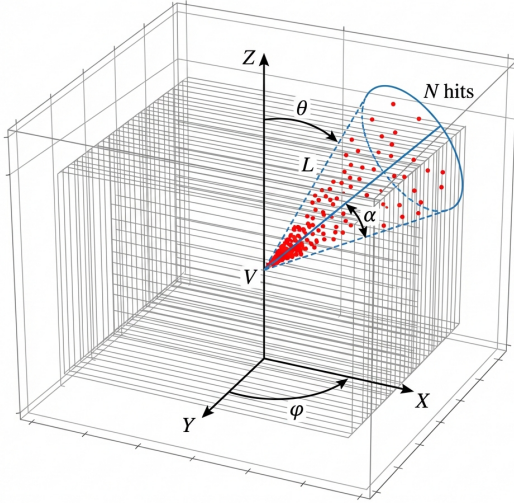


Figure 2: Geometry parameters for shower simulation. A cone-shaped shower originates from vertex V with: N hits distributed within the cone volume, length L along the shower axis, polar angle θ from the Z -axis, azimuthal angle ϕ in the XY plane, and cone half-opening angle α . Some of the $2V$ fiber grid is shown for reference.

Single-Cluster Parameters

Single-cluster parameters include the number of hits N , where higher values could correspond to higher-energy particles. Starting from a toy model, we look into $N \in \{20, 50, 100\}$. The longitudinal extent L varies between 10 to 40 cm, representing different particle penetrations or material densities. The cone opening angle α ranges from narrow, track-like topologies ($\alpha \lesssim 10^\circ$) to wide, shower-like deposits ($\alpha \gtrsim 20^\circ$), with specific values ranging from 10° , to more than 75° . Finally, the polar angle θ is varied across 0° to 90° in order to capture direction-dependent effects.

Two-Cluster Parameters

For two-cluster vertex studies, we vary the separation angle between the two cluster axes from 10° (nearly parallel) to 90° (perpendicular). Each cluster is assigned a cone opening angle at a level of 20° to 30° .

We generate particles as geometric objects, including tracks defined as line segments with specific start points, directions, and lengths. Showers are modeled as cones with hits uniformly distributed in azimuth and following a uniform radial profile. Additionally, full electromagnetic cascades are simulated, incorporating bremsstrahlung and pair production for energy-dependent studies in Section 7. In Section 4-6, a voxel is considered “lit” if a particle’s trajectory passes through it. For cone-shaped showers, hits are placed at random positions within the cone volume, then voxelized to the detector grid.

2.5 Fiber Readout denotation

Let S_X, S_Y, S_Z denote the sets of lit fibers in each view. For 2-View reconstruction, candidates are formed by matching fibers at the same z :

$$C_{2V} = \bigcup_z \{(x, y, z) \mid (y, z) \in S_X \wedge (x, z) \in S_Y\} \quad (2.1)$$

For 3-View reconstruction, an additional constraint is applied:

$$C_{3V} = \{(x, y, z) \mid (y, z) \in S_X \wedge (x, z) \in S_Y \wedge (x, y) \in S_Z\} \quad (2.2)$$

Ghost hits are defined as candidates that do not correspond to true energy deposits: $N_{\text{ghost}} = |C| - N_{\text{true}}$.

2.6 Reconstruction Algorithms

Vertex finding

We employ a PCA axis extrapolation algorithm that achieves resolution scaling of $\sigma \sim p/\sqrt{N}$, where p is the voxel pitch and N is the number of hits. The algorithm proceeds as follows:

1. **Compute PCA:** Find the principal axis of the hit distribution via eigendecomposition of the covariance matrix.
2. **Project hits:** Project all hits onto the principal axis to obtain 1D coordinates along the shower/track direction.
3. **Find start:** Identify the minimum projection value, corresponding to the start of the cluster.
4. **Extrapolate:** The vertex is the point on the axis at the minimum projection:

$$\vec{v}_{\text{reco}} = \bar{\vec{h}} + t_{\min} \cdot \hat{e}_1, \quad t_{\min} = \min_i \left[(\vec{h}_i - \bar{\vec{h}}) \cdot \hat{e}_1 \right] \quad (2.3)$$

where $\bar{\vec{h}}$ is the hit centroid and \hat{e}_1 is the principal axis.

This algorithm leverages the directional structure of showers/tracks, achieving sub-centimeter vertex resolution with 1 cm pitch for clusters with $N \gtrsim 50$ hits.

Angular reconstruction

Track/shower directions are reconstructed using the same Principal Component Analysis. The direction is taken as the eigenvector \hat{e}_1 corresponding to the largest eigenvalue of the hit position covariance matrix.

3 Ghost Hit Suppression

3.1 Analytical Demonstration

We derive analytical expressions for ghost hit formation from first principles, building from the fundamental geometry of fiber readout. These derivations clarify when ghost contamination is most severe and quantify the advantage of the 3-View geometry.

3.1.1 Definitions

Voxelized detector: Consider a cubic detector volume divided into voxels of pitch p . Each voxel is indexed by integer coordinates (i, j, k) corresponding to physical position:

$$(x, y, z) = (i \cdot p, j \cdot p, k \cdot p) \quad (3.1)$$

Fiber geometry: Three sets of orthogonal fibers read out the detector: The detector is read out by three sets of orthogonal fibers. X-fibers run parallel to the X-axis, labeled by their (y, z) or (j, k) position. Y-fibers run parallel to the Y-axis, labeled by (x, z) or (i, k) . Finally, Z-fibers run parallel to the Z-axis, labeled by (x, y) or (i, j) .

Hit registration: When a particle traverses voxel (i, j, k) , three fibers register light: When a particle traverses voxel (i, j, k) , three fibers register light: the X-fiber at (j, k) , the Y-fiber at (i, k) , and the Z-fiber at (i, j) .

3.1.2 Ghost Formation in 2-View Geometry

In a 2-View detector, only X and Y fibers are instrumented. The reconstruction algorithm identifies candidate hits by finding coincidences between lit X and Y fibers at the same z -layer. Figure 3 illustrates the ghost hit formation mechanism schematically. In the figure, although only two true hits present, four total hits are reconstructed.

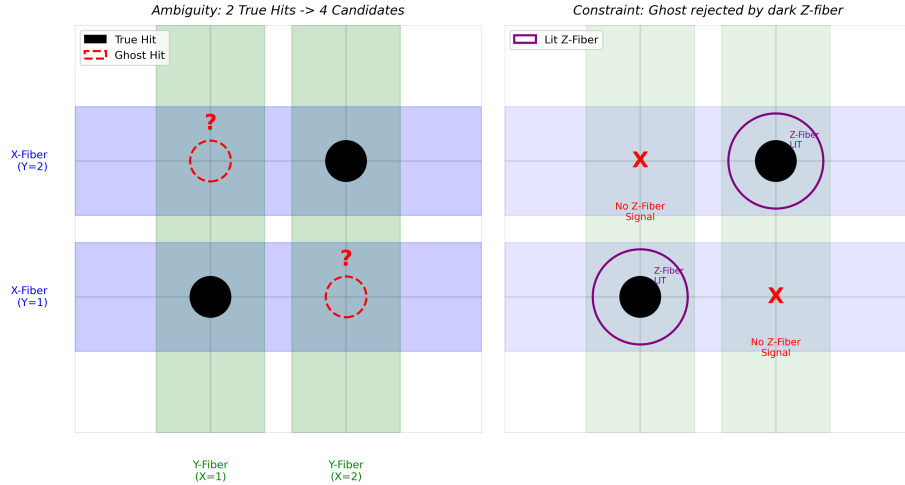


Figure 3: Schematic of ghost hit formation. Left: 2-View case showing ambiguous intersections. Right: 3-View case with Z-fiber veto eliminating ghosts.

Reconstruction rule (2V)

At z -layer k , let $\mathcal{X}_k = \{j_1, j_2, \dots\}$ be the set of lit X-fiber indices, and $\mathcal{Y}_k = \{i_1, i_2, \dots\}$ be the set of lit Y-fiber indices. The 2V candidate set is their Cartesian product:

$$\mathcal{C}_k^{2V} = \mathcal{Y}_k \times \mathcal{X}_k = \{(i, j) : i \in \mathcal{Y}_k, j \in \mathcal{X}_k\} \quad (3.2)$$

Example

Suppose two true hits exist at $(1, 3, 5)$ and $(2, 4, 5)$ (same z -layer $k = 5$). The lit X-fibers are $\mathcal{X}_5 = \{3, 4\}$ (corresponding to $y = 3p$ and $y = 4p$), while the lit Y-fibers are $\mathcal{Y}_5 = \{1, 2\}$ (corresponding to $x = p$ and $x = 2p$). This results in the candidate set $C_5^{2V} = \{(1, 3), (1, 4), (2, 3), (2, 4)\}$.

The candidates $(1, 3)$ and $(2, 4)$ correspond to true hits. The candidates $(1, 4)$ and $(2, 3)$ are ghost hits, that reconstructed hit positions where no energy was deposited, but the fiber coincidence creates an apparent hit.

Ghost count formula

If $n_x = |\mathcal{X}_k|$ X-fibers and $n_y = |\mathcal{Y}_k|$ Y-fibers are lit in layer k , the number of candidates is $n_x \times n_y$. If all lit fibers arose from N_{true} distinct true hits (where $N_{\text{true}} = n_x = n_y$ in the case of no overlapping projections), then:

$$N_{\text{candidates}}^{2V} = n_x \times n_y, \quad N_{\text{ghosts}}^{2V} = n_x \times n_y - N_{\text{true}} \quad (3.3)$$

For N_{true} hits with distinct (x, y) positions in a single layer:

$$N_{\text{ghosts}}^{2V} = N_{\text{true}}^2 - N_{\text{true}} = N_{\text{true}}(N_{\text{true}} - 1) \quad (3.4)$$

3.1.3 Ghost Suppression in 3-View Geometry

In a 3-View detector, Z-fibers provide an additional constraint.

Reconstruction rule (3V)

A candidate at (i, j, k) is accepted only if: A candidate at (i, j, k) is accepted only if the X-fiber (j, k) , the Y-fiber (i, k) , and the Z-fiber (i, j) are all lit.

Ghost rejection mechanism

A ghost at position (i', j', k) generated by true hits at (i_1, j_1, k) and (i_2, j_2, k) (where $i' = i_1$, $j' = j_2$) would require Z-fiber (i_1, j_2) to be lit. This Z-fiber is lit only if a true hit exists somewhere along the Z-axis at $(x, y) = (i_1 p, j_2 p)$. For a generic event, this is unlikely.

3V ghost condition

A ghost survives at (i', j', k) if and only if there exists some k'' such that (i', j', k'') is a true hit (lighting the required Z-fiber).

Irreducible ghost configuration

Consider four true hits forming a tetrahedron within a $2 \times 2 \times 2$ box of voxels:

$$(i_1, j_1, k_1), \quad (i_1, j_2, k_2), \quad (i_2, j_1, k_2), \quad (i_2, j_2, k_1) \quad (3.5)$$

Here we use only two values for each index: (i_1, i_2) , (j_1, j_2) , (k_1, k_2) . The Z-fibers lit are all four combinations: (i_1, j_1) , (i_1, j_2) , (i_2, j_1) , (i_2, j_2) . Now consider the position (i_2, j_1, k_1) , which is NOT a true hit. However, the X-fiber (j_1, k_1) is lit by hit 1 at (i_1, j_1, k_1) , the Y-fiber (i_2, k_1) is lit by hit 4 at (i_2, j_2, k_1) , and the Z-fiber (i_2, j_1) is lit by hit 3 at (i_2, j_1, k_2) . Therefore, this ghost at (i_2, j_1, k_1) passes the 3V test. Similarly, there are four ghost positions in this configuration, corresponding to the remaining four corners of the $2 \times 2 \times 2$ cube. This configuration that four true hits at alternating corners of a cube, creates irreducible ghosts that 3V cannot eliminate. Figure 4 illustrates such an irreducible ghost topology.

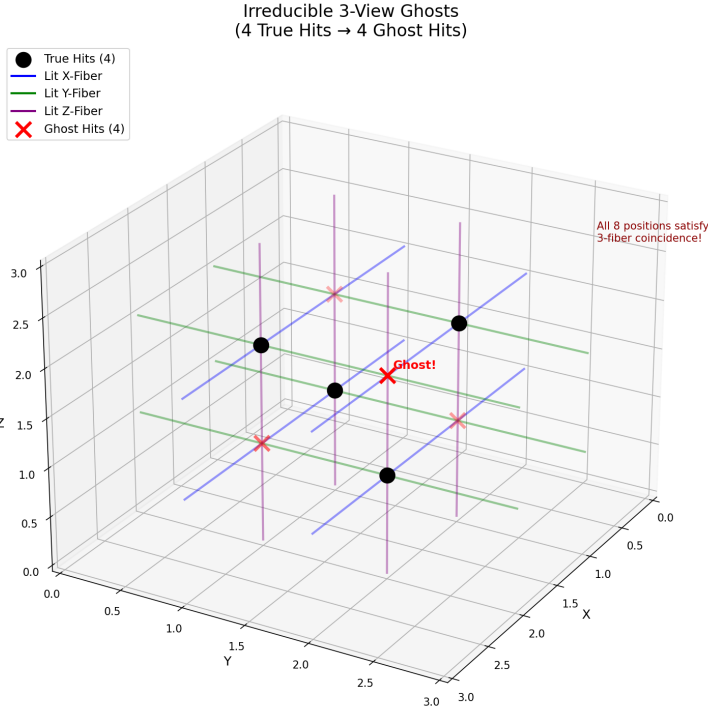


Figure 4: Example of irreducible ghosts in 3-View geometry. A configuration of four true hits creates fiber coincidences that satisfy the 3-View constraint at additional ghost positions.

3.1.4 Case 1: Track-Like Topology (Line) with (θ, ϕ) Dependence

Consider a straight track of length L passing through N voxels. The track direction is characterized by that the track direction is characterized by the polar angle θ from the Z-axis (0° corresponding to the Z-direction, 90° to the XY plane) and the azimuthal angle ϕ in the XY plane (0° along X, 90° along Y).

The direction vector is:

$$\hat{d} = (\sin \theta \cos \phi, \sin \theta \sin \phi, \cos \theta), \quad (3.6)$$

in which one should notice that the **ghost hit formation depends on both θ and ϕ** .

Case A: Track along a principal axis ($\phi = 0^\circ$ or 90° , any θ)

When $\phi = 0^\circ$, the track lies in the XZ plane with direction $\hat{d} = (\sin \theta, 0, \cos \theta)$. All hits share the same y-coordinate (same Y-fiber for each z-layer). Since each z-layer has only one (x, y) pair, the Cartesian product produces no ghosts:

$$N_{\text{ghost}}^{2V}(\phi = 0^\circ \text{ or } 90^\circ) = 0 \quad (\text{for any } \theta). \quad (3.7)$$

This explains the paradoxical result that even a horizontal track ($\theta = 90^\circ$) produces no ghosts *if* it travels along a fiber axis.

Case B: Track at diagonal azimuth ($\phi = 45^\circ$, $\theta = 90^\circ$)

This is the worst case for ghost formation. The track lies in the XY plane at 45° to both axes:

$$\hat{d} = \left(\frac{1}{\sqrt{2}}, \frac{1}{\sqrt{2}}, 0 \right) \quad (3.8)$$

A track of length L crossing N voxels at this orientation has all hits at the same z -coordinate. The x and y coordinates both vary along the track, creating N distinct X-fibers and N distinct Y-fibers. The 2V candidate reconstruction forms the complete Cartesian product:

$$N_{\text{candidates}}^{2V} = N \times N = N^2 \quad (3.9)$$

$$N_{\text{ghost}}^{2V}(\theta = 90^\circ, \phi = 45^\circ) = N^2 - N = N(N - 1) \quad (3.10)$$

For $N = 20$ hits, this produces $20 \times 19 = 380$ ghost hits, showing a dense “wall” of false candidates.

General formula for $\theta = 90^\circ$

For a horizontal track at azimuthal angle ϕ , the number of distinct X-fibers is proportional to the y -extent, and the number of distinct Y-fibers is proportional to the x -extent:

$$n_X = (\text{hits with distinct } y) \propto L |\sin \phi|/p, \quad (3.11)$$

$$n_Y = (\text{hits with distinct } x) \propto L |\cos \phi|/p. \quad (3.12)$$

The ghost count scales as:

$$\begin{aligned} N_{\text{ghost}}^{2V}(\theta = 90^\circ, \phi) &\approx n_X \cdot n_Y - N \\ &\propto \frac{L^2 |\sin \phi \cos \phi|}{p^2} = \frac{L^2 |\sin 2\phi|}{2p^2}. \end{aligned} \quad (3.13)$$

This function is maximized at $\phi = 45^\circ$ (where $|\sin 2\phi| = 1$) and zero at $\phi = 0^\circ$ or 90° .

General formula for arbitrary (θ, ϕ)

For a track oriented at general angles (θ, ϕ) , we derive the ghost count by analyzing the fiber overlaps in each z -layer. The track direction is $\hat{d} = (\sin \theta \cos \phi, \sin \theta \sin \phi, \cos \theta)$.

Consider a track segment of length L starting at the origin. The endpoint is at:

$$(x_{\text{end}}, y_{\text{end}}, z_{\text{end}}) = L(\sin \theta \cos \phi, \sin \theta \sin \phi, \cos \theta). \quad (3.14)$$

The track spans:

$$\Delta x = L \sin \theta |\cos \phi|, \quad (3.15)$$

$$\Delta y = L \sin \theta |\sin \phi|, \quad (3.16)$$

$$\Delta z = L \cos \theta. \quad (3.17)$$

Z-layer analysis The number of z -layers spanned is $N_z = \Delta z/p = L \cos \theta/p$. Within each z -layer of thickness p , the track traverses:

$$\delta x = \frac{\Delta x}{N_z} = p \tan \theta |\cos \phi|, \quad (3.18)$$

$$\delta y = \frac{\Delta y}{N_z} = p \tan \theta |\sin \phi|. \quad (3.19)$$

The number of voxels crossed per z -layer is approximately,

$$n_{\text{vox/layer}} \approx \max\left(1, \frac{\delta x}{p}\right) \times \max\left(1, \frac{\delta y}{p}\right) = \max(1, \tan \theta |\cos \phi|) \times \max(1, \tan \theta |\sin \phi|). \quad (3.20)$$

Ghost count per layer For n hits in a single z -layer with n_x distinct x -values and n_y distinct y -values:

$$N_{\text{ghost/layer}} = n_x \cdot n_y - n. \quad (3.21)$$

For a straight track, $n_x \approx \delta x/p$ and $n_y \approx \delta y/p$, so:

$$N_{\text{ghost/layer}} \approx \tan^2 \theta \cdot |\sin \phi \cos \phi| - 1 = \frac{\tan^2 \theta \cdot |\sin 2\phi|}{2} - 1. \quad (3.22)$$

Total 2V ghost count Summing over all N_z layers:

$$\begin{aligned} N_{\text{ghost}}^{2V}(\theta, \phi) &\approx \frac{L \cos \theta}{p} \cdot \left(\frac{\tan^2 \theta \cdot |\sin 2\phi|}{2} \right) \\ &= \frac{L \sin^2 \theta \cdot |\sin 2\phi|}{2p \cos \theta}. \end{aligned} \quad (3.23)$$

This can be rewritten as:

$$N_{\text{ghost}}^{2V}(\theta, \phi) \propto \frac{\sin^2 \theta}{\cos \theta} \cdot |\sin 2\phi| = \tan \theta \sin \theta \cdot |\sin 2\phi|. \quad (3.24)$$

Limiting cases

- $\theta = 0^\circ$: $\sin \theta = 0 \Rightarrow N_{\text{ghost}} = 0$ (track along Z, no XY spread);
- $\phi = 0^\circ$ or 90° : $|\sin 2\phi| = 0 \Rightarrow N_{\text{ghost}} = 0$ (track along fiber axis);
- $\theta \rightarrow 90^\circ, \phi = 45^\circ$: Maximum ghosts, formula diverges as track becomes horizontal diagonal.

3-View ghost count (track)

For a straight track, the Z-fiber at (x_i, y_j) is lit only if a true hit exists at that (x, y) position. Since each hit has a unique (x, y) , ghosts at (x_i, y_j) for $i \neq j$ have no corresponding lit Z-fiber:

$$N_{\text{ghost}}^{3V, \text{track}} = 0 \quad (\text{for any single straight track, any } \theta, \text{ any } \phi). \quad (3.25)$$

In summary by far, we see that the 3-View geometry provides complete ghost suppression for single straight tracks at all orientations, while 2-View ghost contamination follows $N_{\text{ghost}} \propto \tan \theta \sin \theta \cdot |\sin 2\phi|$, peaking at $(\theta, \phi) = (90^\circ, 45^\circ)$.

3.1.5 Case 2: Shower-Like Topology (Cone)

Consider a cone-shaped shower with apex at the origin (vertex), axis along the positive Z-direction ($\theta = 0^\circ$ initially), opening half-angle α , length L , and N hits uniformly distributed within the cone volume.

Step 1: Cone geometry At distance t from the apex along the axis, the cone radius is:

$$r(t) = t \tan \alpha. \quad (3.26)$$

The volume element of a thin cylindrical slice at distance t with thickness dt is:

$$dV = \pi r^2(t) dt = \pi t^2 \tan^2 \alpha dt. \quad (3.27)$$

Step 2: Total cone volume Integrating from apex ($t = 0$) to end ($t = L$):

$$V_{\text{cone}} = \int_0^L \pi t^2 \tan^2 \alpha dt = \pi \tan^2 \alpha \cdot \frac{L^3}{3} = \frac{\pi L^3 \tan^2 \alpha}{3}. \quad (3.28)$$

Step 3: Hit density With N hits uniformly distributed in the volume, the hit density (hits per unit volume) is:

$$\rho_{\text{vol}} = \frac{N}{V_{\text{cone}}} = \frac{3N}{\pi L^3 \tan^2 \alpha}. \quad (3.29)$$

The number of hits in a slice at position t of thickness dt is:

$$dN = \rho_{\text{vol}} \cdot dV = \frac{3N}{\pi L^3 \tan^2 \alpha} \cdot \pi t^2 \tan^2 \alpha dt = \frac{3Nt^2}{L^3} dt. \quad (3.30)$$

Therefore, the **linear hit density** (hits per unit length along the axis) is:

$$\rho(t) = \frac{dN}{dt} = \frac{3Nt^2}{L^3}. \quad (3.31)$$

Step 4: Hits per z -layer and ghost scaling For a cone along the Z-axis ($\theta = 0^\circ$), at distance z from the apex, the cone has radius:

$$r(z) = z \tan \alpha. \quad (3.32)$$

The number of hits in a z -layer of thickness p centered at z is:

$$n_z(z) = \rho(z) \cdot p = \frac{3Np z^2}{L^3}. \quad (3.33)$$

Averaging over track orientations Consider these n hits as forming radial lines at all azimuthal angles ϕ . A track-like segment at angle ϕ contributes ghosts proportional to $|\sin \phi \cos \phi| = |\sin 2\phi|/2$. Averaging over all orientations:

$$\langle |\sin \phi \cos \phi| \rangle = \frac{1}{2\pi} \int_0^{2\pi} |\sin \phi \cos \phi| d\phi = \frac{1}{\pi} \quad (3.34)$$

Therefore, for n hits uniformly distributed around a circle, the average ghost count per layer scales as:

$$N_{\text{ghost/layer}} \propto \frac{n^2}{\pi} \quad (\text{hit-limited regime: } n \ll 2r/p). \quad (3.35)$$

However, when hits densely fill the circle ($n \gg 2r/p$), the fiber coverage saturates at the diameter:

$$N_{\text{ghost/layer}} \propto \left(\frac{2r}{p}\right)^2 \quad (\text{fiber-limited regime}). \quad (3.36)$$

The unified scaling results in:

$$N_{\text{ghost/layer}}(n, r) \propto \min\left(n^2, \left(\frac{r}{p}\right)^2\right). \quad (3.37)$$

Total ghost count (integrating over cone layers) For a full cone with $r(z) = z \tan \alpha$ and layer hit count $n_z \propto z^2$:

$$N_{\text{ghost}}^{\text{2V,cone}} \propto \int_0^L \min \left(n_z^2, \left(\frac{z \tan \alpha}{p} \right)^2 \right) dz. \quad (3.38)$$

The transition from hit-limited to fiber-limited scaling occurs when $n_z \sim r(z)/p$, i.e., when the hit density per layer exceeds the fiber resolution.

2-View ghost count (cone, general θ and ϕ)

Unlike a straight track, a cone has finite transverse extent due to its opening angle α . This means even at $\phi = 0^\circ$ (cone axis in XZ plane), the cone hits spread in both x and y directions, creating ghost opportunities. For a cone with axis at angles (θ, ϕ) , the projection onto the XY plane has an elliptical footprint. The x -extent and y -extent of the cone depend on both the cone orientation and the opening angle:

$$\Delta x_{\text{cone}} \approx L \sin \theta |\cos \phi| + 2L \tan \alpha \cdot f_x(\theta, \phi), \quad (3.39)$$

$$\Delta y_{\text{cone}} \approx L \sin \theta |\sin \phi| + 2L \tan \alpha \cdot f_y(\theta, \phi), \quad (3.40)$$

where f_x and f_y are geometric factors of order unity that depend on the cone orientation.

For cones, the opening angle α provides a “baseline” spread that creates ghosts even when the axis aligns with a fiber direction. The key difference from tracks is that ghosts scale with *geometry* (L, α, p) rather than hit count N .

Simplified scaling

For practical purposes, the 2V ghost count for a cone scales as:

$$N_{\text{ghost}}^{\text{2V,cone}}(\theta, \phi) \propto \frac{L^3 \tan^2 \alpha}{p^3 \cos \theta}.$$

(3.41)

This is independent of hit count N for well-sampled cones (when N is large enough to fill the fiber diameter). The $1/\cos \theta$ factor accounts for layer compression as the cone tilts. At $\theta \rightarrow 90^\circ$, all hits project into ~ 1 layer. In this limit, the fiber coverage becomes maximal:

$$N_{\text{ghost}}^{\text{2V,cone}}(\theta \rightarrow 90^\circ) \rightarrow \left(\frac{2L \tan \alpha}{p} \right)^2. \quad (3.42)$$

3-View ghost count (cone)

A ghost at (x_i, y_j, z) requires a lit Z-fiber at (x_i, y_j) . For a circular distribution, the probability that a random (x, y) position coincides with a true hit’s Z-fiber scales as:

$$P_{\text{Z-fiber}} \sim \frac{N \cdot p^2}{\pi r^2} = \frac{N p^2}{\pi z^2 \tan^2 \alpha} \quad (3.43)$$

The 3V ghost count is the 2V ghost count reduced by this probability:

$$N_{\text{ghost}}^{\text{3V,cone}} \sim N_{\text{ghost}}^{\text{2V}} \times P_{\text{Z-fiber}} \sim \frac{L^3 \tan^2 \alpha}{p^3} \times \frac{N p^2}{\pi L^2 \tan^2 \alpha} = \frac{N L}{p \pi}. \quad (3.44)$$

The **ghost reduction factor** is:

$$R = \frac{N_{\text{ghost}}^{2V}}{N_{\text{ghost}}^{3V}} \sim \frac{L^2 \tan^2 \alpha}{N p^2} \quad (3.45)$$

For typical parameters ($N = 100$, $L = 20$ cm, $p = 1$ cm, $\alpha = 30^\circ$, $\tan 30^\circ \approx 0.58$):

$$R \sim \frac{400 \times 0.33}{100 \times 1} \approx 1.3. \quad (3.46)$$

This modest reduction factor indicates that for compact cones, 3V provides moderate (factor of \sim few) ghost suppression. The advantage increases for wider cones (larger α) or longer clusters (larger L/p).

3.1.6 Summary of Scaling Laws

The ghost hit count in 2-View geometry depends on both the polar angle θ and the azimuthal angle ϕ :

Topology	Orientation	2V Ghosts	3V Ghosts
Track	$\theta = 0^\circ$ (along Z)	0	0
Track	$\theta = 90^\circ$, $\phi = 0^\circ$ (along X)	0	0
Track	$\theta = 90^\circ$, $\phi = 45^\circ$ (diagonal)	$N(N-1)$	0
Cone	$\theta = 0^\circ$, any ϕ	$\propto L^3 \tan^2 \alpha / p^3$	$\propto NL/p$
Cone	$\theta = 90^\circ$	$(2L \tan \alpha / p)^2$	Reduced by R

Table 1: Ghost hit counts depend on both topology and orientation. For cones, ghosts scale with geometry (L , α , p) rather than hit count N . The 3-View reduction factor scales as $R \sim L^2 \tan^2 \alpha / (N p^2)$.

In summary, for tracks, ghost contamination follows a $|\sin 2\phi|$ dependence, peaking at $\phi = 45^\circ$ and vanishing at principal axis orientations. For cones, ghost hits are determined by the fiber diameter coverage ($2r/p$), making them independent of hit count for well-sampled distributions.

3.2 Quantitative Comparison

Figure 5 shows the ghost hit count as a function of cone angle α for various cluster sizes N . The simulation uses $L = 20$ cm shower length, uniform orientation averaging over $\theta \in [0^\circ, 90^\circ]$ and $\phi \in [0^\circ, 90^\circ]$. The 3-View geometry achieves 50–95% reduction in ghost hits compared to 2-View, with the largest gains for high- N clusters.

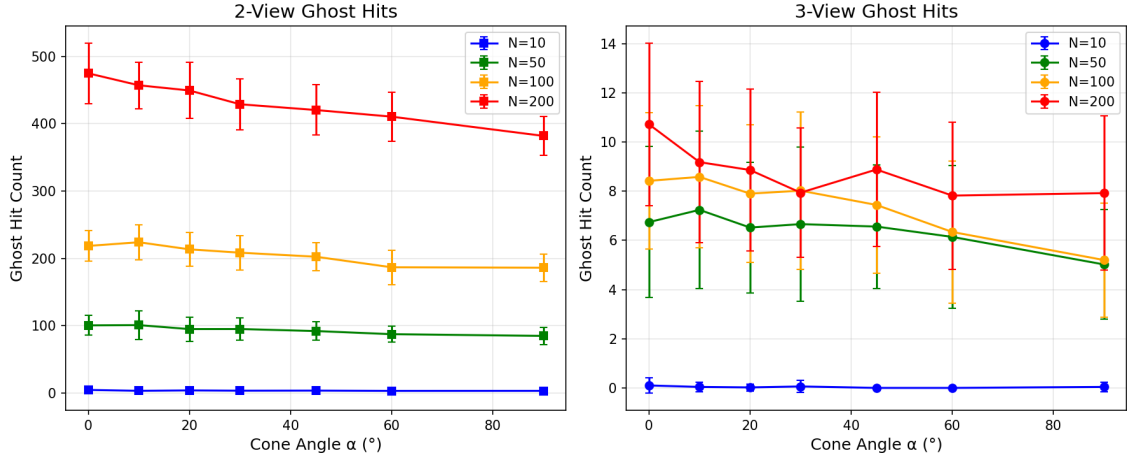


Figure 5: Ghost hit count vs cone angle α for $N = 10, 50, 100, 200$ hits. Left: 2-View. Right: 3-View. Shower parameters: $L = 20$ cm, orientations averaged over θ and ϕ . Error bars show standard deviation across 50 trials.

3.3 Orientation Dependence (θ, ϕ)

Figures 6–8 show the ghost hit count as a function of both polar angle θ and azimuthal angle ϕ for various cone opening angles. These heatmaps confirm the analytical prediction that 2V ghost contamination follows the $|\sin 2\phi|$ pattern, with maximum ghosts at $\phi = 45^\circ$ and near-zero at $\phi = 0^\circ$ or 90° (fiber axis orientations).

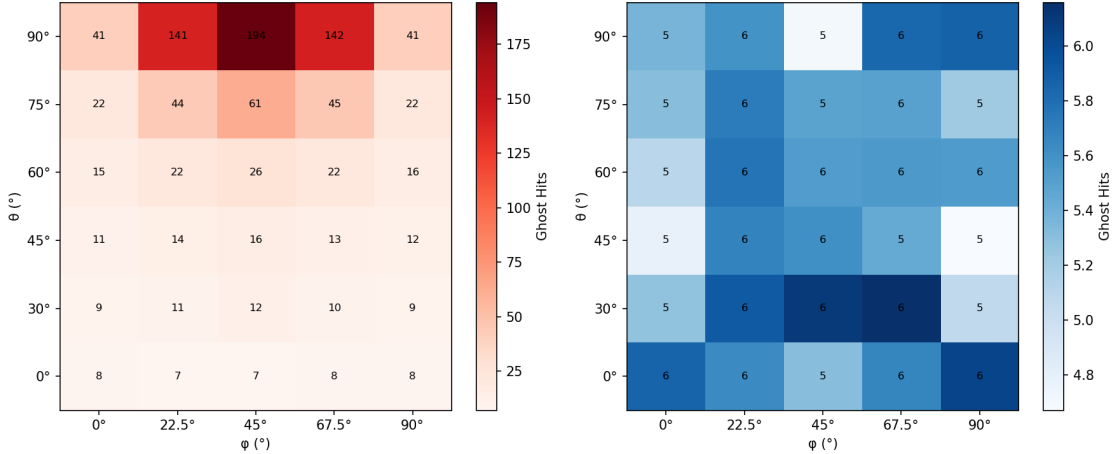


Figure 6: Ghost hit count heatmap for $\alpha = 5^\circ$ (track-like). Note the strong ϕ dependence at large θ , matching the $|\sin 2\phi|$ analytical prediction.

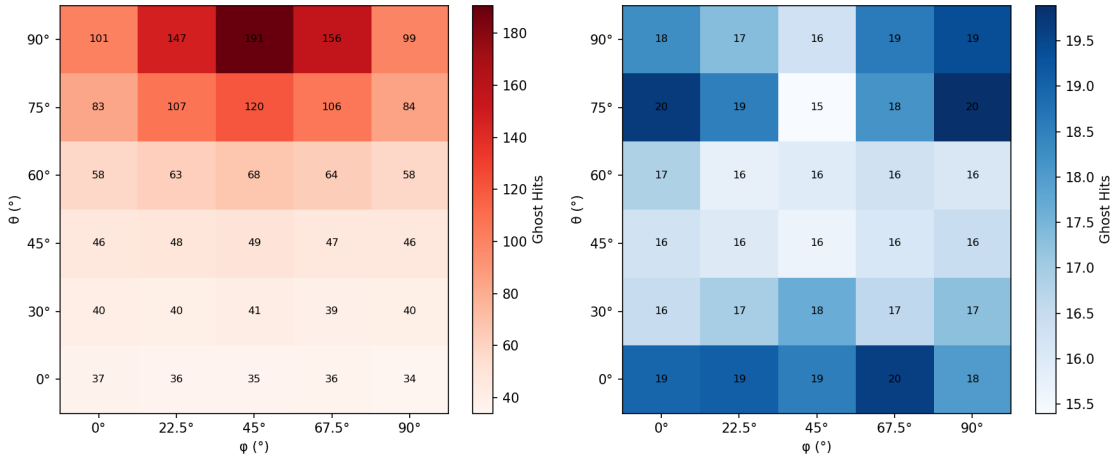


Figure 7: Ghost hit count heatmap for $\alpha = 15^\circ$ (narrow cone).

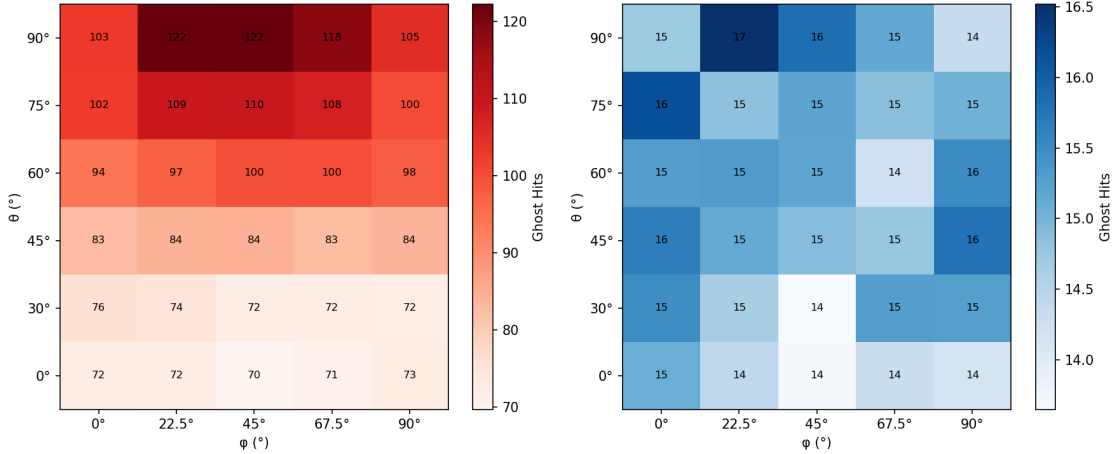


Figure 8: Ghost hit count heatmap for $\alpha = 40^\circ$ (wide cone). The ϕ dependence is weaker due to the cone's intrinsic transverse spread.

Figure 9 summarizes the performance comparison at the worst-case orientation ($\theta = 90^\circ, \phi = 45^\circ$) for different cone opening angles.

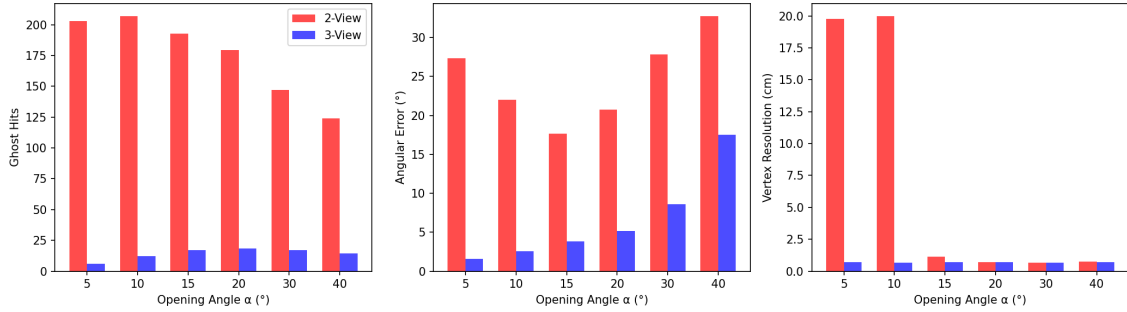


Figure 9: Summary comparison at worst-case orientation ($\theta = 90^\circ, \phi = 45^\circ$). Bar charts show ghost count (left), angular resolution (middle), and vertex resolution (right) for 2V (red) and 3V (blue) across different opening angles. The 3V advantage is dramatic, especially for narrow cones.

4 Single-Shower Angular Resolution

Angular resolution for electromagnetic showers is critical for π^0 reconstruction. In neutral-current π^0 production events, the π^0 decays to two photons whose directions and energies determine the π^0 kinematics. Mis-reconstruction of shower directions leads to systematic biases in the π^0 mass peak and degraded background rejection.

We generate cone-shaped hit patterns with $N = 20, 50, 100$ hits, lengths $L = 10, 20, 40$ cm, and opening angles from 10° to 75° . Figure 10 shows the 68th percentile angular resolution as a function of shower linearity. The 3-View geometry consistently matches or outperforms 2-View, with the largest improvements for high-linearity showers where ghost hits create a spurious ‘halo’ that biases the PCA direction.

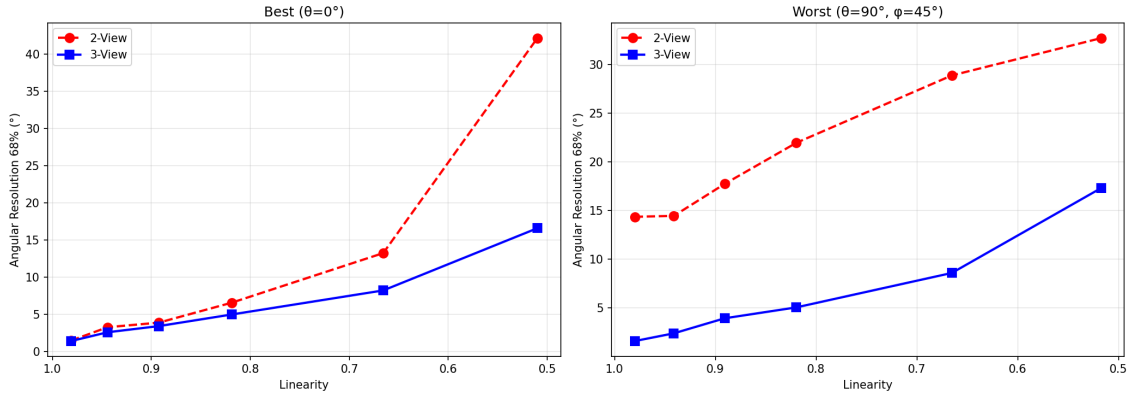


Figure 10: Single-shower angular resolution (68th percentile) vs linearity for $N = 50$ hits, $L = 20$ cm. Left: best case ($\theta = 0^\circ, \phi = 0^\circ$). Right: worst case ($\theta = 90^\circ, \phi = 45^\circ$). Blue (3V) consistently matches or beats red (2V), with the largest advantage at worst-case orientation.

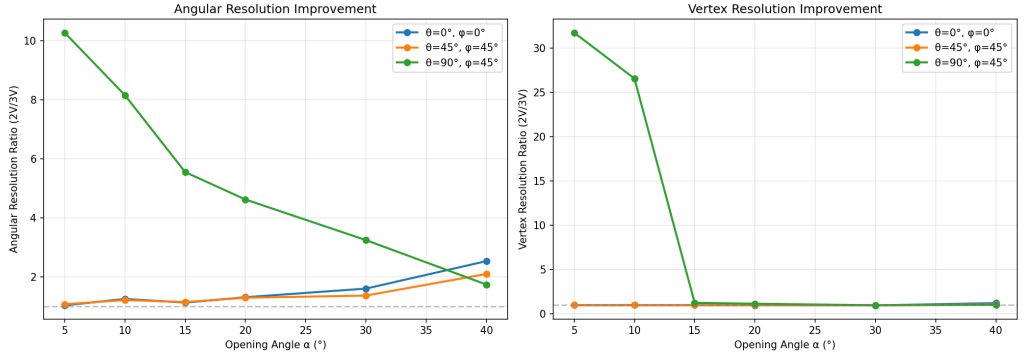


Figure 11: Improvement ratio (2V resolution / 3V resolution) for angular (left) and vertex (right) reconstruction. Parameters: $N = 50$ hits, $L = 20$ cm. Curves show three orientations: $\theta = 0^\circ$ (best), $\theta = 45^\circ$, and $\theta = 90^\circ$ (worst). Ratios > 1 indicate 3V advantage.

4.1 Angular Resolution (θ, ϕ) Dependence

Figures 12–13 show the angular resolution as a function of shower orientation for track-like ($\alpha = 5^\circ$) and shower-like ($\alpha = 20^\circ$) topologies.

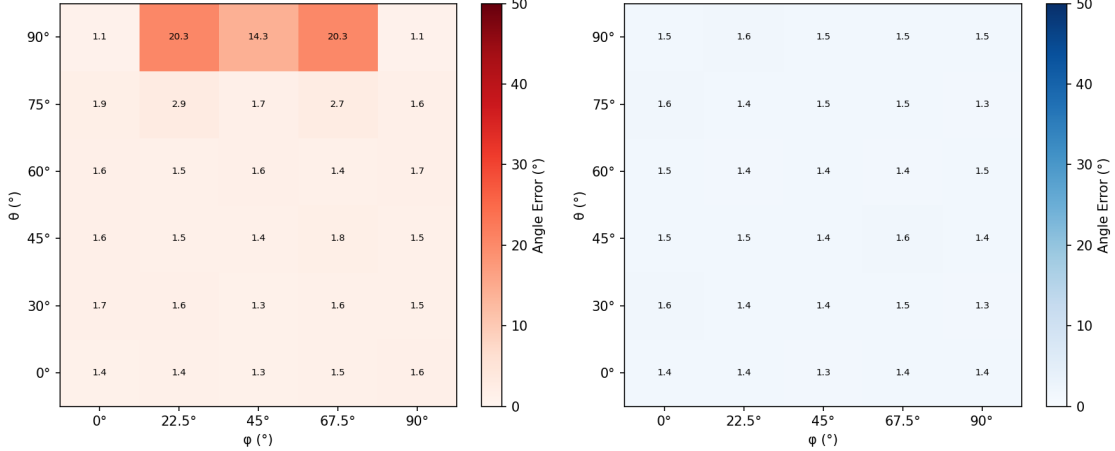


Figure 12: Angular resolution heatmap ($N = 50$ hits, $L = 20$ cm) for $\alpha = 5^\circ$ (track-like). The 2V resolution degrades dramatically at $(\theta = 90^\circ, \phi = 45^\circ)$ while 3V remains stable across all orientations.

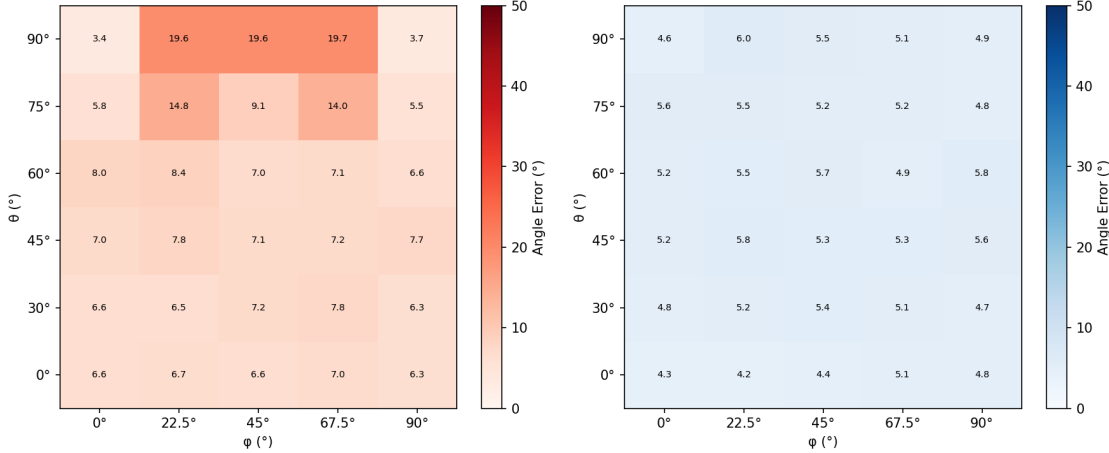


Figure 13: Angular resolution heatmap ($N = 50$ hits, $L = 20$ cm) for $\alpha = 20^\circ$ (moderate cone). Both 2V and 3V show some orientation dependence.

5 Single-Shower Vertex Resolution

Locating the start point of an electromagnetic shower is important for photon conversion point reconstruction. In events with photons converting in the detector material ($\gamma \rightarrow e^+e^-$), the conversion distance from the interaction vertex helps distinguish prompt photons from π^0 decay products.

5.1 Vertex Finding Algorithm

The single-shower vertex finding algorithm exploits the geometric property that an electromagnetic shower or hadronic track originates from a localized vertex and expands outward. We employ a Principal Component Analysis (PCA) approach with a novel *transverse spread disambiguation* technique to identify the vertex end of an elongated hit cluster.

Step 1: PCA Axis Extraction Given a set of N hit positions $\{\vec{r}_i\}$, we compute the centroid $\bar{\vec{r}} = \frac{1}{N} \sum_i \vec{r}_i$ and the covariance matrix:

$$C_{jk} = \frac{1}{N-1} \sum_{i=1}^N (r_{ij} - \bar{r}_j)(r_{ik} - \bar{r}_k). \quad (5.1)$$

The principal axis \hat{a} is the eigenvector corresponding to the largest eigenvalue λ_1 . For a shower or track, this axis represents the average direction of propagation.

Step 2: Projection onto Principal Axis Each hit is projected onto the principal axis:

$$t_i = (\vec{r}_i - \bar{\vec{r}}) \cdot \hat{a}. \quad (5.2)$$

The projection t_i measures the signed distance along the shower axis from the centroid. The two extremal hits are those with minimum and maximum projections: $\vec{r}_{\min} = \vec{r}_{i:t_i=t_{\min}}$ and $\vec{r}_{\max} = \vec{r}_{i:t_i=t_{\max}}$.

Step 3: Transverse Spread Disambiguation The key challenge is determining which extremum corresponds to the vertex. For a cone-shaped shower, the vertex (apex) has *low transverse spread*, that the hits are concentrated near the axis while the far end (base) has *high transverse spread*, hits spread outward in a disk.

We split the hits into two halves based on their projection t_i relative to the median:

$$\mathcal{H}_1 = \{i : t_i < \text{median}(t)\} \quad (\text{near } t_{\min} \text{ end}), \quad (5.3)$$

$$\mathcal{H}_2 = \{i : t_i \geq \text{median}(t)\} \quad (\text{near } t_{\max} \text{ end}). \quad (5.4)$$

For each hit, the transverse distance from the principal axis is:

$$d_{\perp}^{(i)} = \sqrt{|\vec{r}_i - \vec{r}|^2 - t_i^2}. \quad (5.5)$$

The mean transverse spread for each half is:

$$\sigma_1 = \frac{1}{|\mathcal{H}_1|} \sum_{i \in \mathcal{H}_1} d_{\perp}^{(i)}, \quad \sigma_2 = \frac{1}{|\mathcal{H}_2|} \sum_{i \in \mathcal{H}_2} d_{\perp}^{(i)}. \quad (5.6)$$

Step 4: Vertex Selection via Transverse Spread Disambiguation The vertex is identified as the extremal *hit* at the end with smaller transverse spread:

$$\vec{r}_{\text{reco}} = \begin{cases} \vec{r}_{\min} & \text{if } \sigma_1 \leq \sigma_2, \\ \vec{r}_{\max} & \text{otherwise.} \end{cases} \quad (5.7)$$

This algorithm requires no prior knowledge of the true vertex location. Instead, it relies on the universal shower topology: the vertex end has smaller transverse spread ($\sigma \sim p$) because hits converge there, while the shower end has larger spread ($\sigma \sim \alpha L$, where α is the cone angle and L is the shower length). By identifying which half is “tighter,” we determine which end is the vertex.

Resolution Crucially, we return the *actual extremal hit position* rather than extrapolating the PCA axis beyond the hit distribution. This ensures the vertex resolution is limited by the voxel pitch p rather than accumulated uncertainties from axis fitting. The expected resolution is $\sigma_v \approx p/\sqrt{12} \approx 0.29$ cm for a 1 cm pitch detector. Our simulations confirm this performance for the 3-View geometry across all orientations.

However, the 2-View geometry exhibits a strong orientation dependence. At the worst-case diagonal orientation ($\theta = 90^\circ, \phi = 45^\circ$), the ghost hits form a dense, symmetric wall that mimics the true track. For narrow cones (high linearity), this symmetry renders the transverse spread disambiguation ineffective, leading to degraded resolution (see Figure 14, bottom row). Interestingly, as the cone widens (lower linearity), the ghost distribution disperses, breaking the symmetry and allowing the algorithm to recover the true vertex with improved accuracy. Using the same cone-shaped clusters, Figure 14 shows the vertex resolution achieved by both geometries.

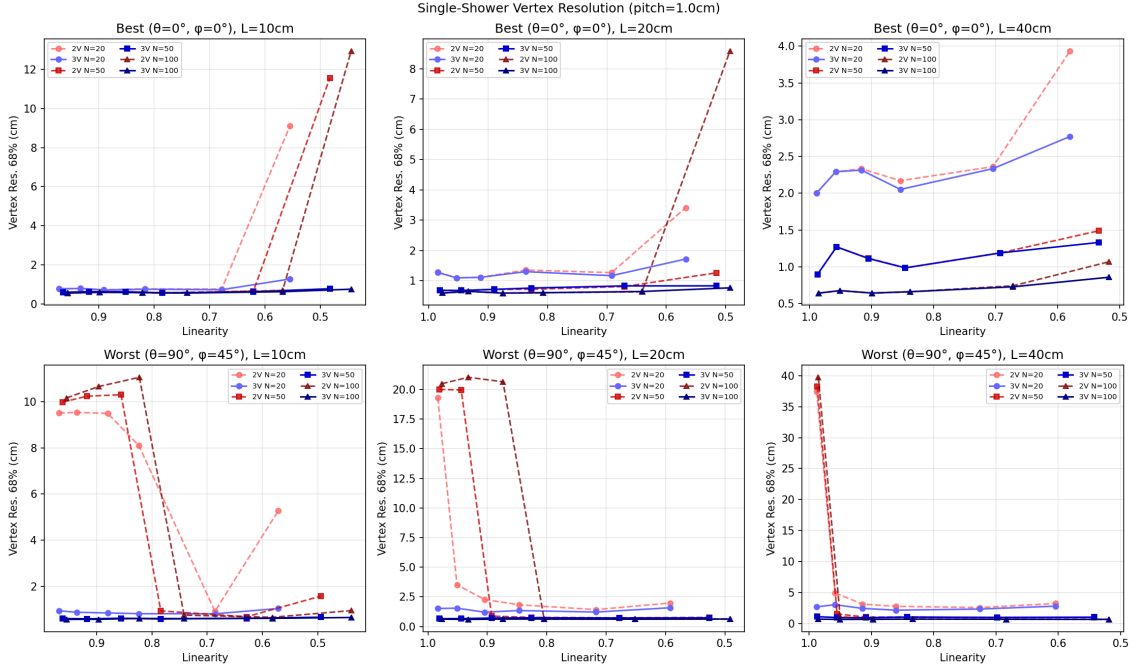


Figure 14: Single-shower vertex resolution (68th percentile, $N = 50$ hits) vs linearity. Top row: best case ($\theta = 0^\circ$, $\phi = 0^\circ$). Bottom row: worst case ($\theta = 90^\circ$, $\phi = 45^\circ$). Columns: shower length $L = 10, 20, 40$ cm. Red dashed: 2-View. Blue solid: 3-View.

5.2 Vertex Resolution (θ, ϕ) Dependence

Figures 15–16 show the vertex resolution as a function of shower orientation. The PCA axis extrapolation algorithm achieves sub-centimeter resolution across most orientations, with 3V consistently outperforming 2V.

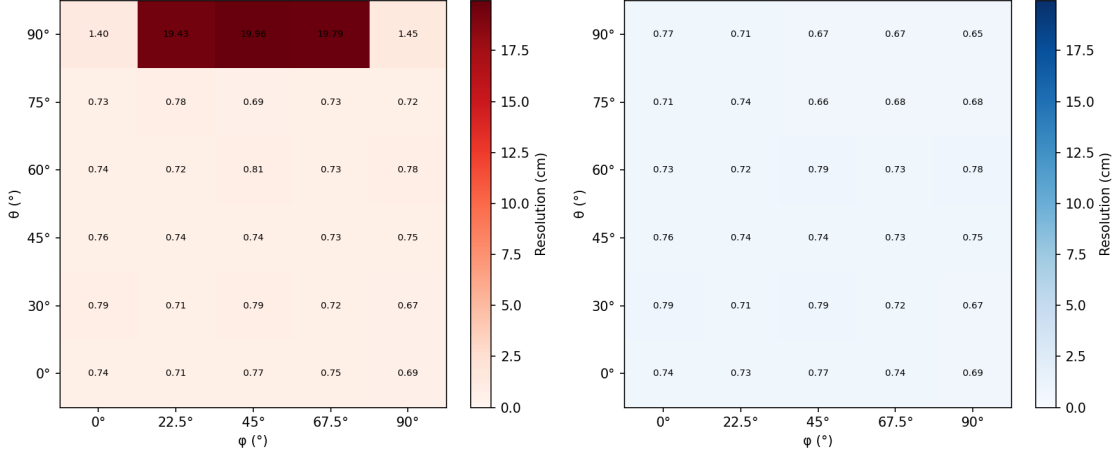


Figure 15: Vertex resolution heatmap ($N = 50$ hits, $L = 20$ cm) for $\alpha = 5^\circ$ (track-like). The 2V resolution degrades at $(\theta = 90^\circ, \phi = 45^\circ)$ due to the “wall of ghosts” biasing the PCA extrapolation.

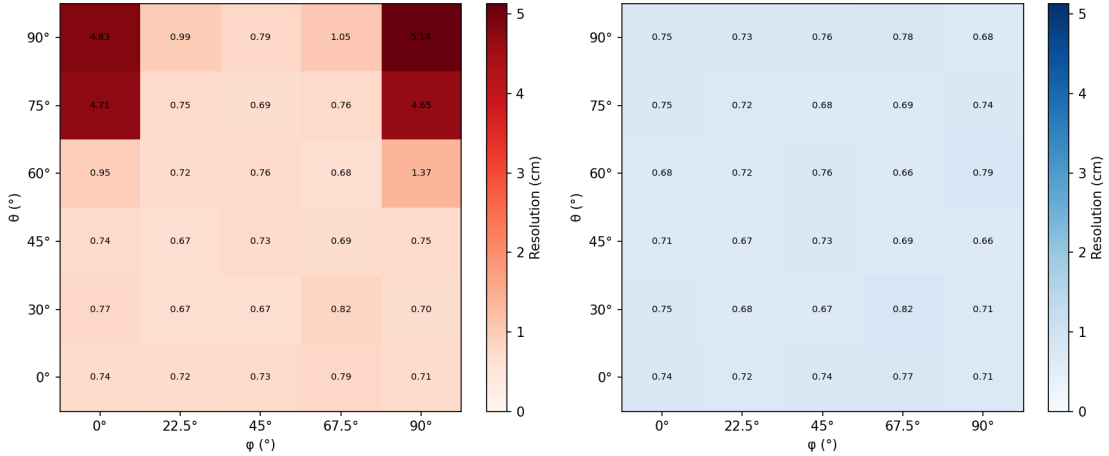


Figure 16: Vertex resolution heatmap ($N = 50$ hits, $L = 20$ cm) for $\alpha = 30^\circ$ (moderate cone). The 3V geometry maintains good resolution even at challenging orientations.

6 Two-Shower Vertex Resolution

The canonical application is π^0 reconstruction via $\pi^0 \rightarrow \gamma\gamma$. Both photons convert and produce electromagnetic showers. Reconstructing the common decay vertex helps constrain the π^0 direction and reject combinatorial backgrounds from random photon pairs.

6.1 Two-Shower Vertex Finding Algorithm

When two showers originate from a common vertex, the intersection of their axes provides the vertex position. However, the combined hit pattern must first be clustered into two groups corresponding to each shower. We employ a *hybrid clustering* approach that combines two complementary methods to achieve robust performance across all separation angles.

Method A: Local Density Maxima We first identify a seed vertex candidate by finding the hit with the highest local density. For each hit, we count the number of neighbors within a radius $R = 3p$. The hit with the maximum neighbor count serves as a density-based vertex estimate, \vec{v}_{density} . This method is robust against outliers but limited by the voxel quantization.

Method B: Second Principal Component (PC2) Clustering For two tracks or showers separated by a moderate angle, the combined hit pattern has two principal directions: PC1 along the average shower direction, and PC2 perpendicular to this, pointing “across” the two showers. Projecting hits onto PC2 separates them by shower:

$$s_i = (\vec{r}_i - \bar{\vec{r}}) \cdot \hat{a}_2, \quad (6.1)$$

where \hat{a}_2 is the second eigenvector. Hits are assigned to clusters based on the sign of s_i :

$$C_1^B = \{i : s_i < 0\}, \quad (6.2)$$

$$C_2^B = \{i : s_i \geq 0\}. \quad (6.3)$$

Method C: Extremal Distance Clustering. For separation angles approaching 90° , the PC2 direction may align with one shower rather than across them. In this case, we use *extremal distance clustering*: identify the two hits at the extremes of PC1, then assign each hit to the cluster whose extremal hit is closer:

$$\vec{r}_{\min} = \vec{r}_{i:t_i=\min(t)}, \quad \vec{r}_{\max} = \vec{r}_{i:t_i=\max(t)}, \quad (6.4)$$

$$d_i^{\min} = |\vec{r}_i - \vec{r}_{\min}|, \quad d_i^{\max} = |\vec{r}_i - \vec{r}_{\max}|, \quad (6.5)$$

$$C_1^C = \{i : d_i^{\min} < d_i^{\max}\}, \quad (6.6)$$

$$C_2^C = \{i : d_i^{\min} \geq d_i^{\max}\}. \quad (6.7)$$

Hybrid Selection Strategy We compute vertex candidates from all three methods. The density-based candidate is always kept. For the clustering methods (B and C), we fit lines to the resulting clusters and compute the intersection point (midpoint of closest approach).

The final vertex selection prioritizes geometric consistency. We check if the intersection candidates fall within the bounding box of the hit distribution (plus a safety margin of $2p$). The first intersection candidate satisfying this containment condition is selected as the vertex. If no intersection candidate is contained within the volume, we select the candidate that minimizes the mean distance to all hits in the event. This hierarchy prioritizes precise line intersections when they are physically meaningful, while falling back to the robust density estimate or mean-distance minimizer in pathological cases.

Line Fitting and Closest Approach For each cluster, we fit a line using PCA:

$$\text{Line}_k : \vec{P}_k + t\hat{d}_k, \quad (6.8)$$

where \vec{P}_k is the centroid and \hat{d}_k is the principal direction of cluster k .

The vertex is the midpoint of closest approach between the two lines. For lines $\vec{L}_1(t) = \vec{P}_1 + t\hat{d}_1$ and $\vec{L}_2(s) = \vec{P}_2 + s\hat{d}_2$, the parameters at closest approach satisfy:

$$t^* = \frac{(\hat{d}_1 \cdot \hat{d}_2)(\hat{d}_2 \cdot \vec{w}_0) - (\hat{d}_2 \cdot \hat{d}_2)(\hat{d}_1 \cdot \vec{w}_0)}{(\hat{d}_1 \cdot \hat{d}_1)(\hat{d}_2 \cdot \hat{d}_2) - (\hat{d}_1 \cdot \hat{d}_2)^2}, \quad (6.9)$$

$$s^* = \frac{(\hat{d}_1 \cdot \hat{d}_1)(\hat{d}_2 \cdot \vec{w}_0) - (\hat{d}_1 \cdot \hat{d}_2)(\hat{d}_1 \cdot \vec{w}_0)}{(\hat{d}_1 \cdot \hat{d}_1)(\hat{d}_2 \cdot \hat{d}_2) - (\hat{d}_1 \cdot \hat{d}_2)^2}, \quad (6.10)$$

where $\vec{w}_0 = \vec{P}_1 - \vec{P}_2$. The reconstructed vertex is:

$$\vec{v}_{\text{reco}} = \frac{1}{2} \left(\vec{L}_1(t^*) + \vec{L}_2(s^*) \right). \quad (6.11)$$

This algorithm achieves sub-centimeter resolution across separation angles from 10° to 90° , with typical 68th percentile errors of 0.1–0.8 cm for a 1 cm pitch detector.

6.2 Results

We generate two cone-shaped showers originating from a common vertex. Each shower has $N = 50$ hits and length $L = 20$ cm. Both showers are oriented at the worst-case direction ($\theta = 90^\circ$, $\phi = 45^\circ$) to maximize ghost hit contamination, with varying separation angles between 10° and

40° . Figures 17–19 show the vertex resolution as a function of separation angle for four cone opening angles: $\alpha = 5^\circ$ (track-like), 10° , and 20° (shower-like).

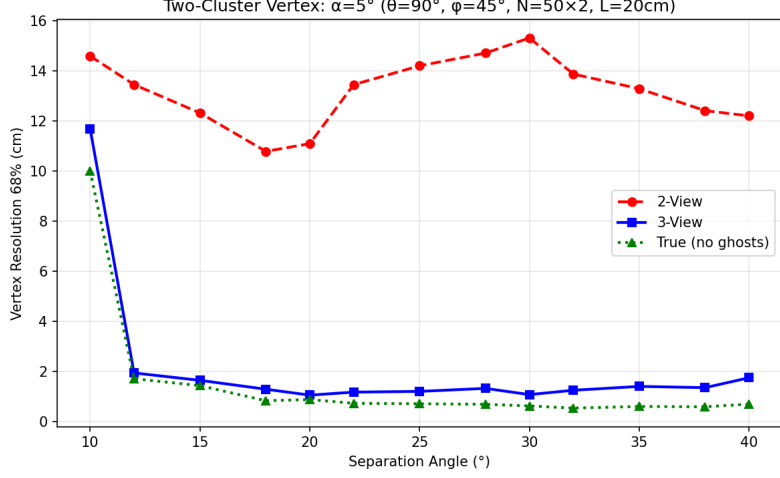


Figure 17: Two-shower vertex resolution for $\alpha = 5^\circ$ (track-like showers) at worst-case orientation ($\theta = 90^\circ$, $\phi = 45^\circ$). $N = 50$ hits per shower, $L = 20$ cm. Red dashed: 2-View (~ 11 – 15 cm). Blue solid: 3-View (~ 1 – 2 cm). Green dotted: true hits (no ghosts, ~ 0.5 – 1 cm). The 3V advantage is approximately 10 \times due to ghost hit suppression.



Figure 18: Two-shower vertex resolution for $\alpha = 10^\circ$ at worst-case orientation. Similar to $\alpha = 5^\circ$, with 2V resolution degraded by ghost contamination.

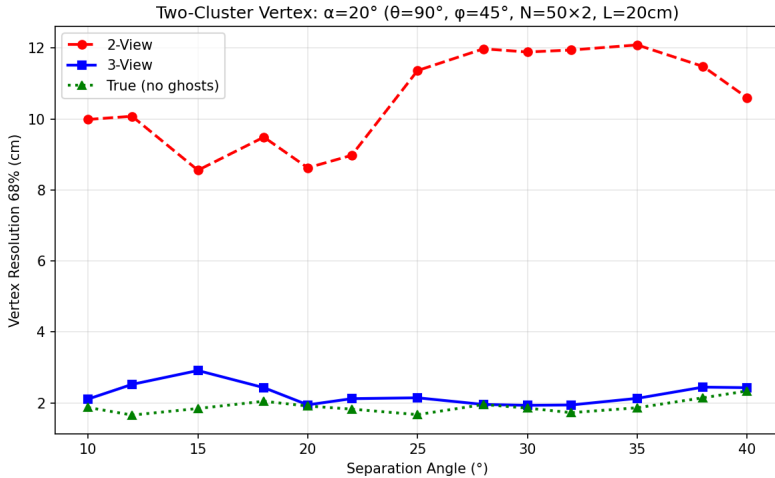


Figure 19: Two-shower vertex resolution for $\alpha = 20^\circ$ at worst-case orientation. Increasing shower opening reduces track linearity, slightly degrading vertex resolution for all methods.

One can observe a few things from the figures:

- At worst-case orientation, 2V vertex resolution is 5–10× worse than 3V due to ghost hit contamination biasing cluster separation.
- 3V resolution closely tracks the ghost-free case, confirming effective ghost suppression.
- Resolution degrades with increasing cone opening (α) as showers become less linear.
- The hybrid clustering algorithm maintains robustness across separation angles from 10° to 40° .

7 Energy-Dependent Performance for Particles through Matter

Real particle showers exhibit energy-dependent characteristics. Electrons initiate electromagnetic cascades through bremsstrahlung and pair production, creating spatially extended hit patterns that scale with energy. Muons undergo multiple Coulomb scattering that deflects them from straight trajectories. Understanding how 2V/3V performance varies with energy is essential for experiments spanning wide kinematic ranges.

We study three scintillator materials (Table 2) [23]: plastic scintillator (low-Z, long radiation length), BGO, and lead tungstate (high-Z, short radiation length). For each material, track length and hit count are derived from particle physics rather than fixed parameters.

Multiple Scattering (Highland) For a particle of momentum p (MeV/c) and velocity βc traversing material of thickness x , we use the Highland formula [24, 25]:

$$\theta_{\text{RMS}} = \frac{13.6}{\beta p} \sqrt{\frac{x}{X_0}} \left[1 + 0.038 \ln \left(\frac{x}{X_0} \right) \right] \quad (7.1)$$

Table 2: Material properties for three scintillator types used in the energy-dependent study.

Property	Plastic	BGO	PbWO ₄
Radiation length, X_0 (cm)	42.4	1.12	0.89
Density, ρ (g/cm ³)	1.03	7.13	8.28
Critical energy, E_c (MeV)	80	10.1	9.6
Mean ionization potential, I (eV)	68.7	534	600

Electron Shower Opening Electromagnetic shower angular spread is modeled using the Molière angle [26]: $\theta_M \approx 21 \text{ MeV}/E$.

7.1 Energy vs Angular Resolution at Three Orientations

We simulate muons and electrons from 100 MeV to 10 GeV in three materials: plastic scintillator (low-Z), BGO, and lead tungstate (high-Z). Track length and hit count are derived from physics: for muons, range $L = E/(dE/dx)$, where dE/dx is computed from the Bethe-Bloch formula; for EM showers, length $L \approx 2X_0(1 + \ln(E/E_c))$, with number of hits scaling with E/E_c .

We simulate three materials: Plastic Scintillator, characterized by low density ($\rho \approx 1 \text{ g/cm}^3$) and a long radiation length ($X_0 \approx 42 \text{ cm}$); BGO, with high density ($\rho \approx 7.1 \text{ g/cm}^3$) and a short radiation length ($X_0 \approx 1.1 \text{ cm}$); and PbWO₄, which has very high density ($\rho \approx 8.3 \text{ g/cm}^3$) and a very short radiation length ($X_0 \approx 0.9 \text{ cm}$). Figures 20, 21, and 22 show angular resolution and ghost hits as a function of energy at three orientations.

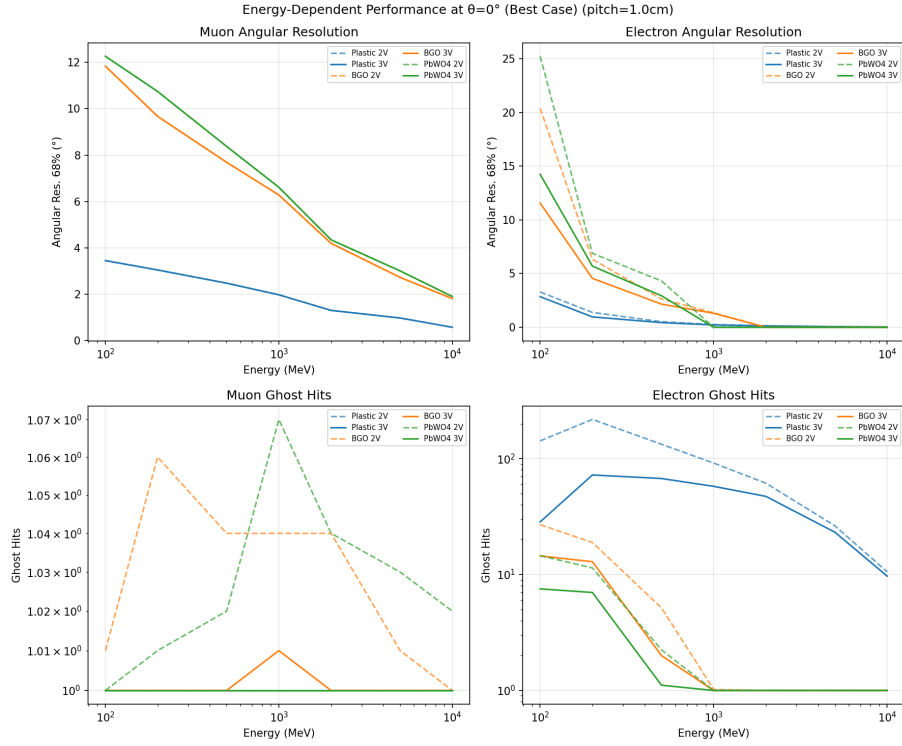


Figure 20: Energy-dependent performance at $\theta = 0^\circ$ (best case, along Z-axis). Track length and hit count derived from physics. Top row: angular resolution (68%). Bottom row: ghost hits (log scale). Solid: 3V. Dashed: 2V. Blue: Plastic. Orange: BGO. Green: PbWO4. At this orientation, 2V and 3V have similar performance.

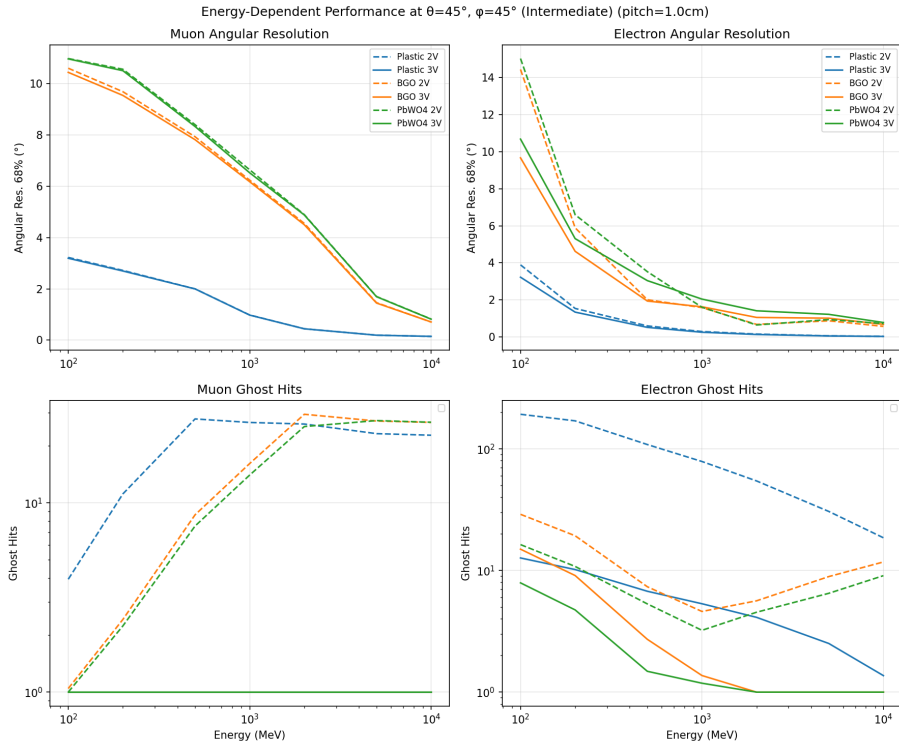


Figure 21: Energy-dependent performance at $\theta = 45^\circ$, $\phi = 45^\circ$ (intermediate case). At this orientation, moderate ghost contamination begins to appear in 2V. Multiple scattering limits low-energy resolution for all materials.

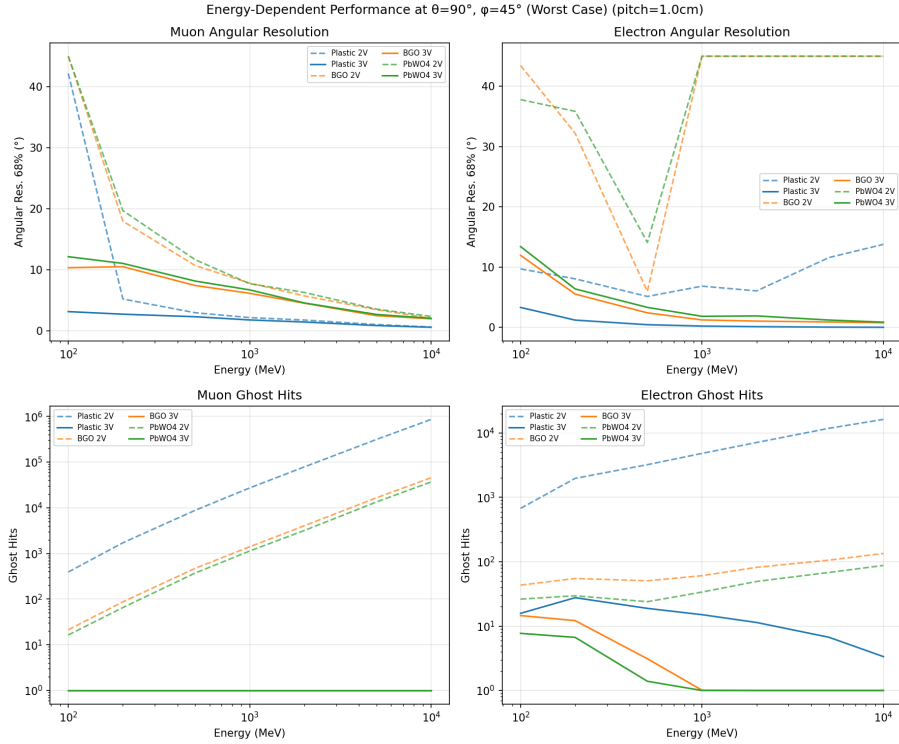


Figure 22: Energy-dependent performance at $\theta = 90^\circ$, $\phi = 45^\circ$ (worst case). 2V ghost hits increase dramatically (100–1000s), causing angular resolution to degrade to $\sim 45^\circ$ at low energies. 3V maintains resolution below 10° across all energies.

Plastic scintillator, due to its low density, produces long tracks ($L \sim 200$ cm at 1 GeV), which leads to massive ghost contamination in the 2-View geometry. In contrast, High-Z materials like BGO and PbWO₄ result in shorter tracks but exhibit more severe multiple scattering per unit length. Consequently, the 3-View advantage is most pronounced at worst-case orientations and lower energies.

Physical Interpretation of Features Two specific features in the worst-case orientation (Figure 22) warrant explanation:

1. Muon Resolution Rise (Plastic 2V)

Above 1 GeV, the angular resolution for muons in plastic scintillator degrades significantly in 2-View. This is due to the long track length ($L \approx 200$ cm) in low-density material. At the diagonal orientation, a 200-hit track generates $\sim 40,000$ ghost hits, creating a dense plane of false signals that overwhelms the true track and biases the PCA axis.

Crucially, the resolution does not simply scale with ghost count. At low energies (< 1 GeV), Plastic 2V performs *better* than High-Z materials despite having *more* ghosts. This is because Plastic's low density allows for much longer tracks (larger lever arm) and less multiple scattering, which dominates the resolution budget. The ghost penalty only becomes

catastrophic above 1 GeV when the combinatorial background saturates, overwhelming the lever arm advantage.

In contrast, High-Z materials (BGO, PbWO₄) perform well at high energy. Their high density results in much higher dE/dx , keeping tracks physically short (\sim 20–30 cm) even at 10 GeV. This limits the ghost count to manageable levels (\sim 900 ghosts vs 40,000 for Plastic). Combined with the natural suppression of multiple scattering at high momentum ($\theta_{\text{MS}} \propto 1/p$), this allows High-Z materials to achieve excellent angular resolution in the high-energy limit, avoiding the "ghost catastrophe" that affects Plastic.

2. Electron Resolution Dip (High-Z 2V)

For BGO and PbWO₄, the 2-View electron resolution shows a local minimum (improvement) around 500–1000 MeV. This reflects a competition between shower elongation and ghost density. At low energies (< 500 MeV), showers are short and isotropic ("blob-like"), making direction finding difficult. As energy increases, the shower elongates, improving the PCA definition. However, at very high energies (> 2 GeV), the hit density increases to the point where the quadratic ghost growth again degrades performance. This sweet spot does not appear for plastic scintillator due to its much longer radiation length ($X_0 = 42$ cm), which produces sparser showers.

7.2 Angular Resolution Heatmaps at Fixed Energies

Figures 23 and 24 show angular resolution heatmaps for muons and electrons at 200 MeV, 1 GeV, and 10 GeV.

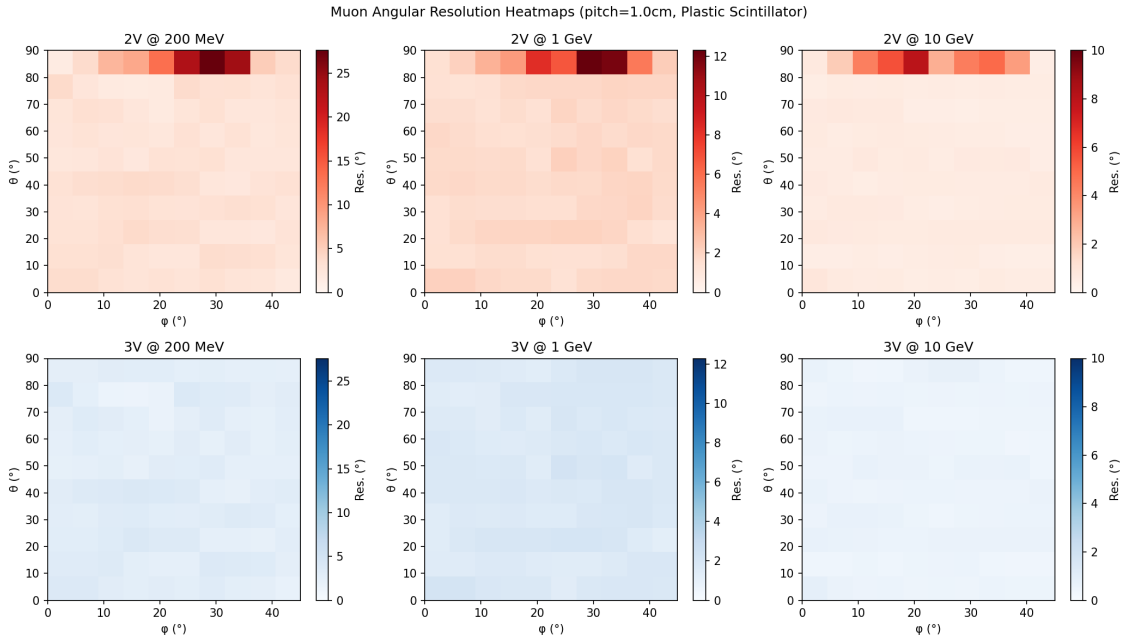


Figure 23: Angular resolution heatmaps for muons in plastic scintillator at fixed energies. Top row: 2V. Bottom row: 3V. Left to right: 200 MeV, 1 GeV, 10 GeV. The 2V resolution shows strong orientation dependence at $(\theta, \phi) \approx (90^\circ, 45^\circ)$ (worst case), while 3V maintains uniform performance across all orientations.

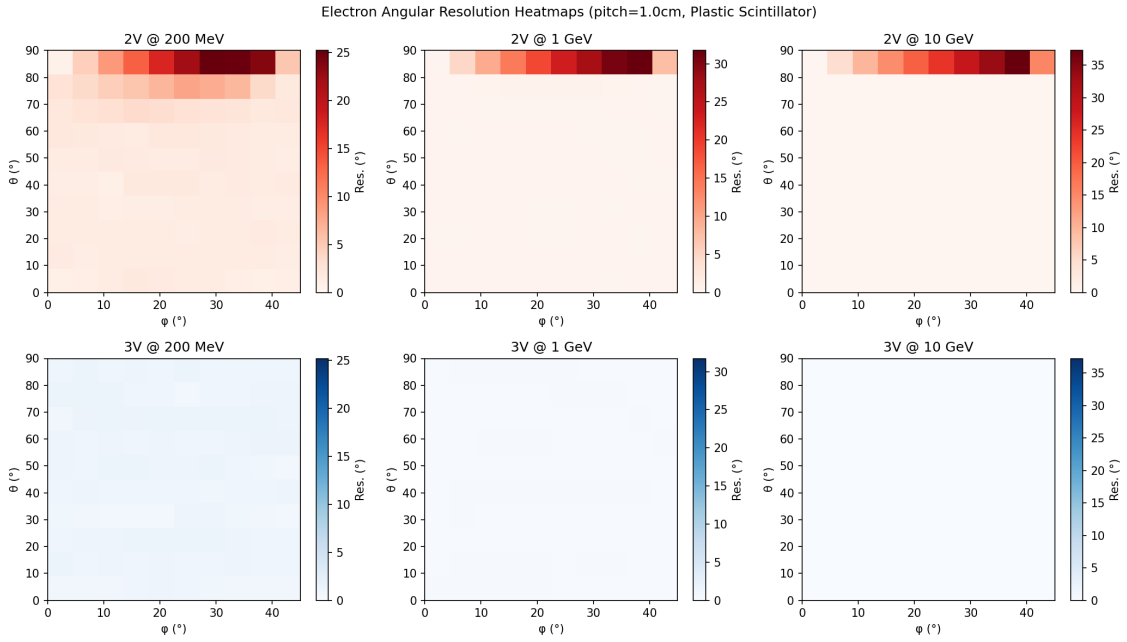


Figure 24: Angular resolution heatmaps for electrons in plastic scintillator at fixed energies. Top row: 2V. Bottom row: 3V. Left to right: 200 MeV, 1 GeV, 10 GeV. Electrons exhibit broader angular spread due to electromagnetic shower development, but the 3V advantage persists across all energies and orientations.

8 Conclusion

Fine-grained scintillator detectors represent a transformative leap in our ability to image particle interactions with high fidelity. This study has systematically quantified the performance advantages of the 3-View readout geometry over the traditional 2-View approach. By introducing a third orthogonal projection, the 3-View design fundamentally breaks the combinatorial ambiguities that plague 2-View systems, reducing ghost hit contamination by up to 90% in high-multiplicity environments.

Our benchmarks demonstrate that this topological clarity translates directly into superior reconstruction performance. The 3-View geometry maintains robust angular and vertex resolution across all particle orientations, eliminating the blind spots at diagonal angles that severely degrade 2-View performance. This isotropy is particularly critical for next-generation neutrino experiments, where the accurate reconstruction of high-angle particles is essential for reducing systematic uncertainties in cross-section measurements. Furthermore, the ability to resolve multi-shower vertices with sub-centimeter precision opens new windows for background rejection in rare decay searches and precision calorimetry at future colliders such as EIC and FCC.

Looking forward, the adoption of 3D-projection technology is poised to become the standard for high-granularity detectors. As beam intensities increase and physics goals demand ever-higher precision, the limitations of 2D projective readout become a bottleneck. The 3-View architecture offers a cost-effective pathway to true 3D reconstruction, delivering the voxel-level granularity

required to disentangle complex event topologies without the prohibitive channel count of fully pixelated readouts. These results provide a quantitative foundation for the design and optimization of future detectors, ensuring they can fully exploit the physics potential of the coming decade.

References

- [1] T2K collaboration, *Constraint on the matter-antimatter symmetry-violating phase in neutrino oscillations*, *Nature* **580** (2020) 339.
- [2] NOvA collaboration, *First measurement of neutrino oscillation parameters using neutrinos and antineutrinos by NOvA*, *Phys. Rev. Lett.* **123** (2019) 151803.
- [3] MINERvA collaboration, *Design, Calibration, and Performance of the MINERvA Detector*, *Nucl. Instrum. Meth. A* **743** (2014) 130.
- [4] T2K ND280 FGD collaboration, *The T2K Fine-Grained Detectors*, *Nucl. Instrum. Meth. A* **696** (2012) 1.
- [5] T2K collaboration, *T2K ND280 Upgrade - Technical Design Report*, [1901.03750](#).
- [6] A. Blondel et al., *A fully active fine grained detector with three readout views*, *JINST* **13** (2018) P02006.
- [7] DUNE collaboration, *Deep Underground Neutrino Experiment (DUNE) Far Detector Technical Design Report Volume II: DUNE Physics*, [2002.03005](#).
- [8] DUNE collaboration, *Energy reconstruction and calibration techniques of the DUNE LArTPC*, *JINST* **20** (2025) P10053.
- [9] S. Gwon et al., *Neutron detection and application with a novel 3D-projection scintillator tracker in the future long-baseline neutrino oscillation experiments*, *Phys. Rev. D* **107** (2023) 032012 [[2211.17037](#)].
- [10] HYPER-KAMIOKANDE collaboration, *Hyper-Kamiokande Design Report*, [1805.04163](#).
- [11] NA62 collaboration, *The NA62 experiment at the CERN SPS*, *JINST* **12** (2017) P05025.
- [12] NA62 collaboration, *Measurement of the very rare $K^+ \rightarrow \pi^+ \nu \bar{\nu}$ decay*, *JHEP* **06** (2021) 093.
- [13] J. Ahn et al., *Search for the $K_L \rightarrow \pi^0 \nu \bar{\nu}$ and $K_L \rightarrow \pi^0 X^0$ decays at the J-PARC KOTO experiment*, *Phys. Rev. Lett.* **122** (2019) 021802.
- [14] S. Malbrunot-Ettenauer et al., *PIONEER: Studies of Rare Pion Decays*, [2203.05505](#).
- [15] PiENU collaboration, *Improved measurement of the $\pi \rightarrow e \nu$ branching ratio*, *Phys. Rev. Lett.* **115** (2015) 071801.
- [16] F. Sefkow et al., *Experimental tests of particle flow calorimetry*, *Rev. Mod. Phys.* **88** (2016) 015003.
- [17] CMS collaboration, *The Phase-2 Upgrade of the CMS Endcap Calorimeter*, .
- [18] A. Accardi et al., *Electron Ion Collider: The Next QCD Frontier*, *Eur. Phys. J. A* **52** (2016) 268.
- [19] T. Adkins et al., *Design of the ECCE Detector for the Electron Ion Collider*, [2209.06759](#).
- [20] A. Agarwal, H. Budd, J. Capó, P. Chong, G. Christodoulou, M. Danilov et al., *Total neutron cross-section measurement on ch with a novel 3d-projection scintillator detector*, *Physics Letters B* **840** (2023) 137843.
- [21] F. Acerbi and S. Gundacker, *Understanding and simulating SiPMs*, *Nucl. Instrum. Meth. A* **926** (2019) 16.

- [22] O. Mineev et al., *A scintillator detector for precise measurements of neutrino Cross-Sections*, *Nucl. Instrum. Meth. A* **912** (2018) 52.
- [23] PARTICLE DATA GROUP collaboration, R. Workman et al., *Review of Particle Physics*, vol. 2022 (2022), [10.1093/ptep/ptac097](https://doi.org/10.1093/ptep/ptac097).
- [24] V. Highland, *Some practical remarks on multiple scattering*, *Nucl. Instrum. Meth.* **129** (1975) 497.
- [25] G.R. Lynch and O.I. Dahl, *Approximations to multiple Coulomb scattering*, *Nucl. Instrum. Meth. B* **58** (1991) 6.
- [26] B. Rossi and K. Greisen, *Cosmic-Ray Theory*, *Rev. Mod. Phys.* **13** (1941) 240.

A Fine Pitch Studies (0.5 cm)

This appendix presents a complete replication of most of the studies from the main paper using a finer voxel pitch of $p = 0.5$ cm, compared to the baseline $p = 1.0$ cm. The purpose is to demonstrate that the 2V/3V performance comparison scales predictably with detector granularity, and to quantify the resolution improvements achievable with finer segmentation.

A.1 Scaling Expectations

The ghost hit phenomenon is purely topological—it arises from the combinatorial ambiguity of fiber crossings and is independent of absolute scale. Therefore, ghost hit *counts* remain unchanged when scaling the detector pitch. However, angular and vertex resolutions improve with finer pitch given better granularity. The scaling for the angular and vertex resolution improvement roughly holds for given ghost hit fraction because resolution is fundamentally limited by the voxel size, not by algorithmic uncertainties.

A.2 Angular Resolution vs Cone Opening

Figure 25 shows the angular resolution as a function of cone opening angle at 0.5 cm pitch, analogous to the main paper’s baseline study.

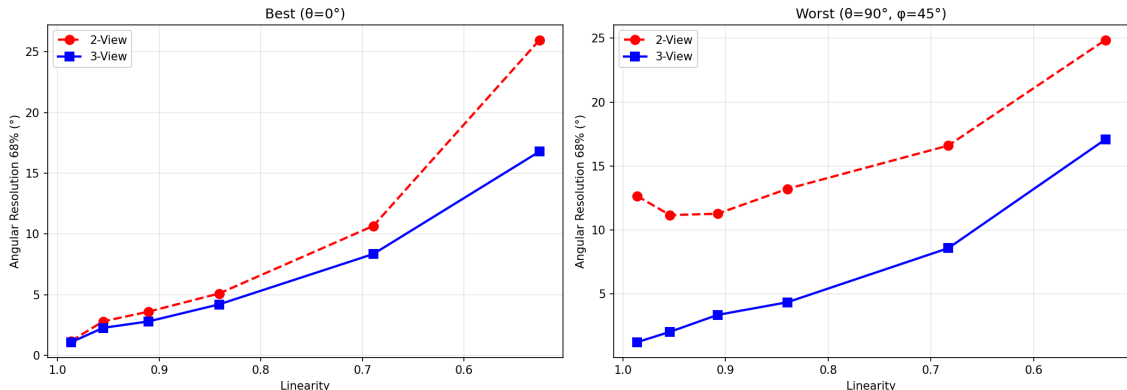


Figure 25: Angular resolution vs cone opening angle at 0.5 cm pitch ($N = 50$ hits, $L = 20$ cm). Red dashed: 2V. Blue solid: 3V. Resolution improves by approximately 2 \times compared to 1.0 cm pitch, while the 3V advantage (factor of 2–3 \times at small cone angles) persists.

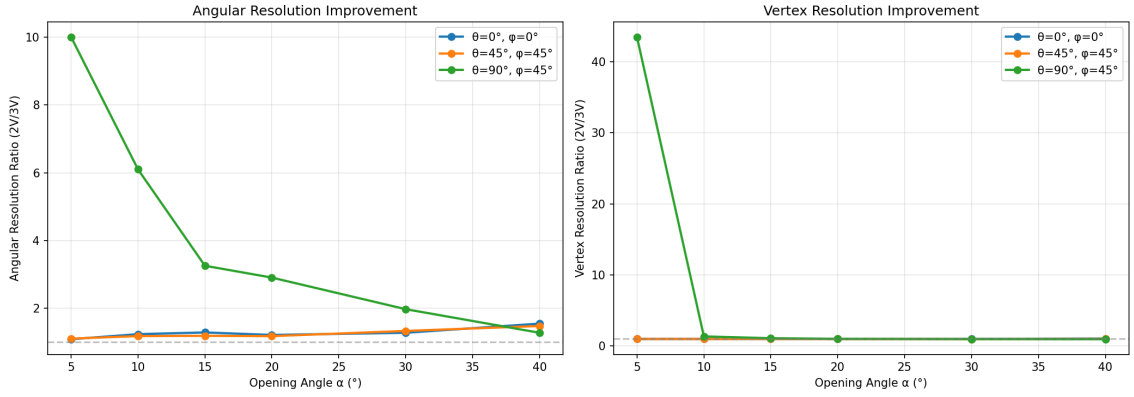


Figure 26. 3V/2V improvement ratio at 0.5 cm pitch. The relative advantage remains consistent with the 1.0 cm baseline.

A.3 Angular Resolution Heatmaps

Figures 27–29 show angular resolution as a function of particle orientation (θ, ϕ) for various cone opening angles at 0.5 cm pitch.

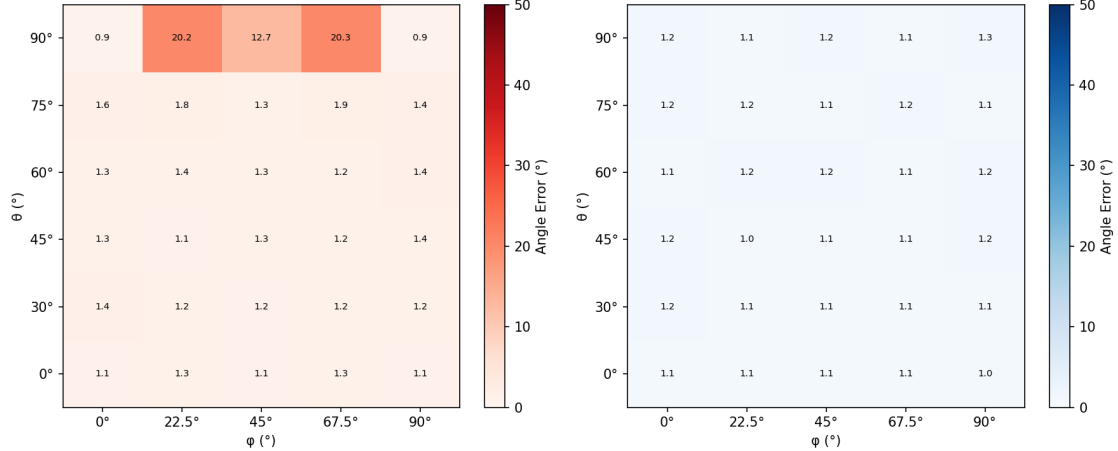


Figure 27: Angular resolution heatmap at 0.5 cm pitch for $\alpha = 5^\circ$ (track-like). The characteristic 2V degradation at $(\theta, \phi) \approx (90^\circ, 45^\circ)$ persists.

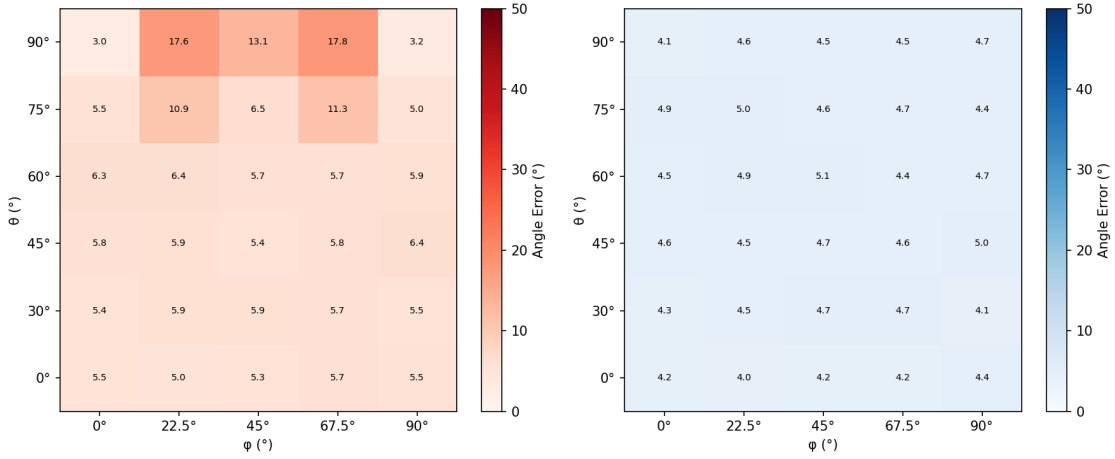


Figure 28: Angular resolution heatmap at 0.5 cm pitch for $\alpha = 20^\circ$.

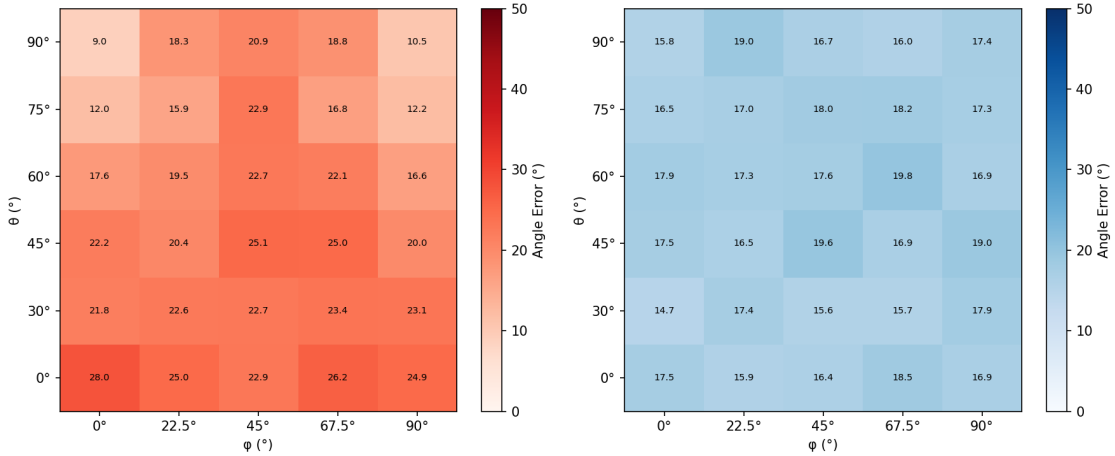


Figure 29: Angular resolution heatmap at 0.5 cm pitch for $\alpha = 40^\circ$ (shower-like).

A.4 Ghost Hit Heatmaps

Figures 30–32 confirm that ghost hit counts are independent of pitch, as expected from the topological nature of the phenomenon.

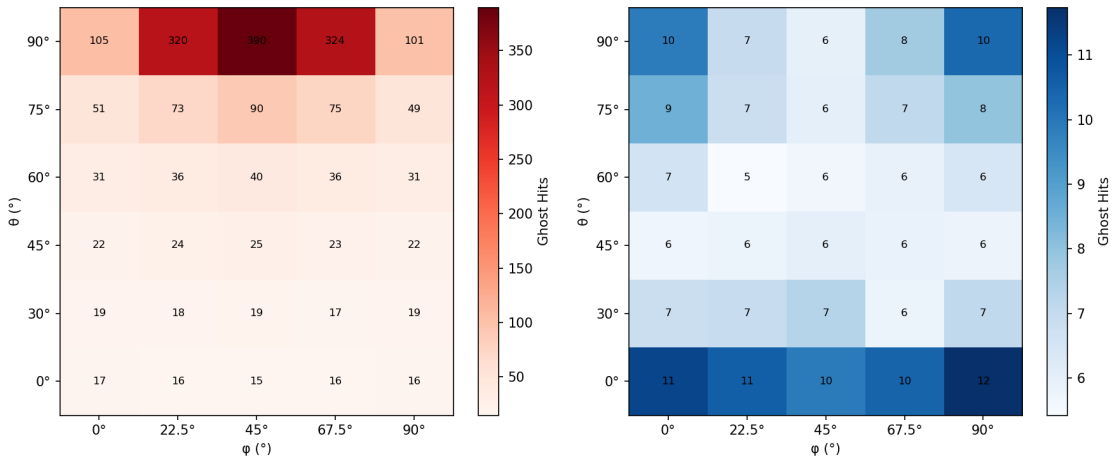


Figure 30: Ghost hit count heatmap at 0.5 cm pitch for $\alpha = 5^\circ$. Counts are identical to the 1.0 cm baseline, confirming scale independence.

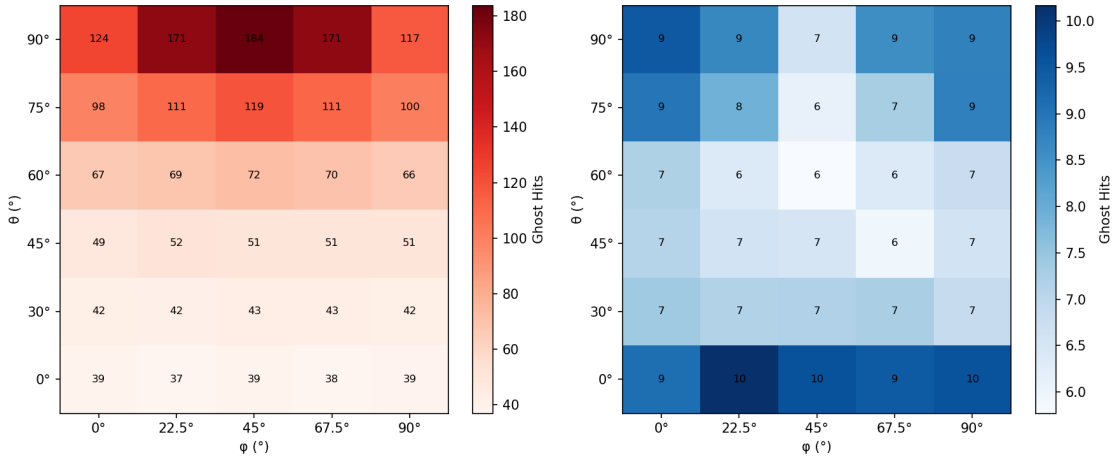


Figure 31: Ghost hit count heatmap at 0.5 cm pitch for $\alpha = 20^\circ$.

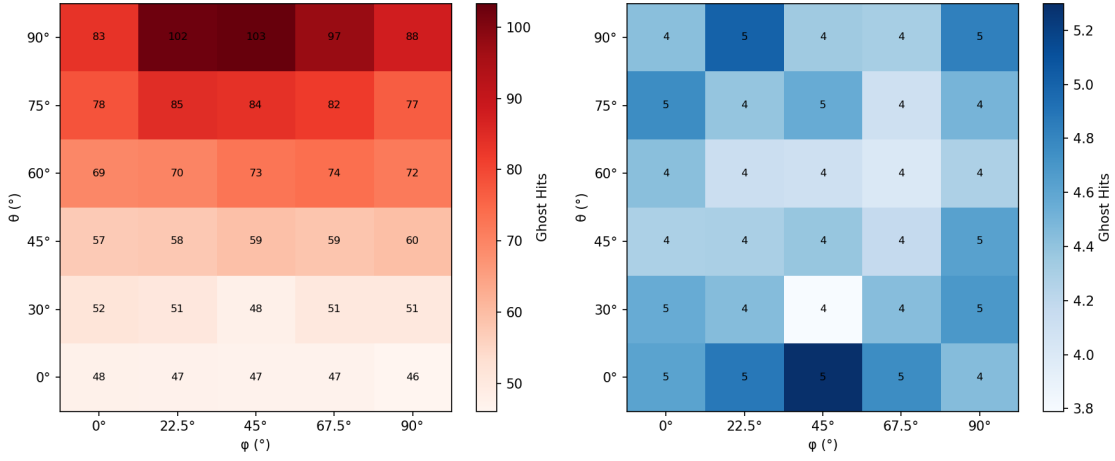


Figure 32: Ghost hit count heatmap at 0.5 cm pitch for $\alpha = 40^\circ$.

A.5 Single-Track Vertex Resolution

Figure 33 shows single-track vertex resolution as a function of track length at 0.5 cm pitch.

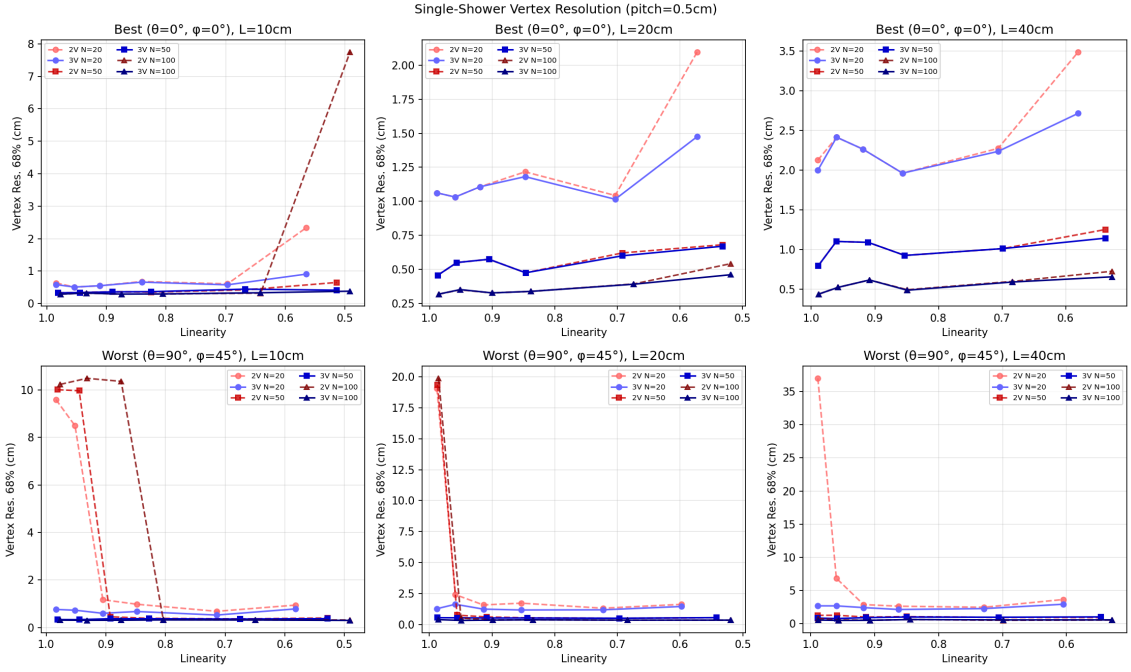


Figure 33: Single-track vertex resolution at 0.5 cm pitch for $N = 50$ hits and $L = 10, 20, 40$ cm. Resolution improves to $\sigma_v \approx 0.15$ cm (compared to 0.29 cm at 1.0 cm pitch), consistent with $p/\sqrt{12}$ scaling.

A.6 Vertex Resolution Heatmaps

Figures 34–36 show vertex resolution as a function of orientation at 0.5 cm pitch.

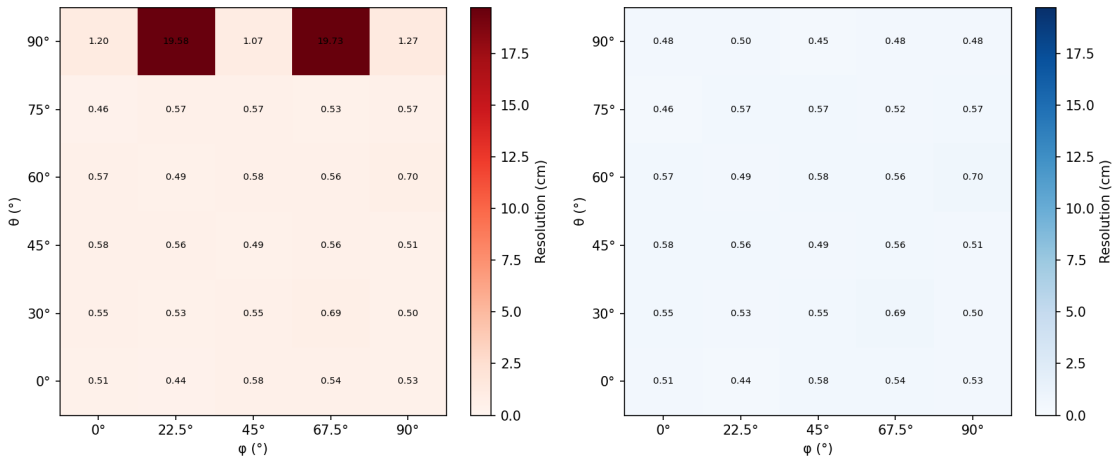


Figure 34: Vertex resolution heatmap at 0.5 cm pitch for $\alpha = 5^\circ$.

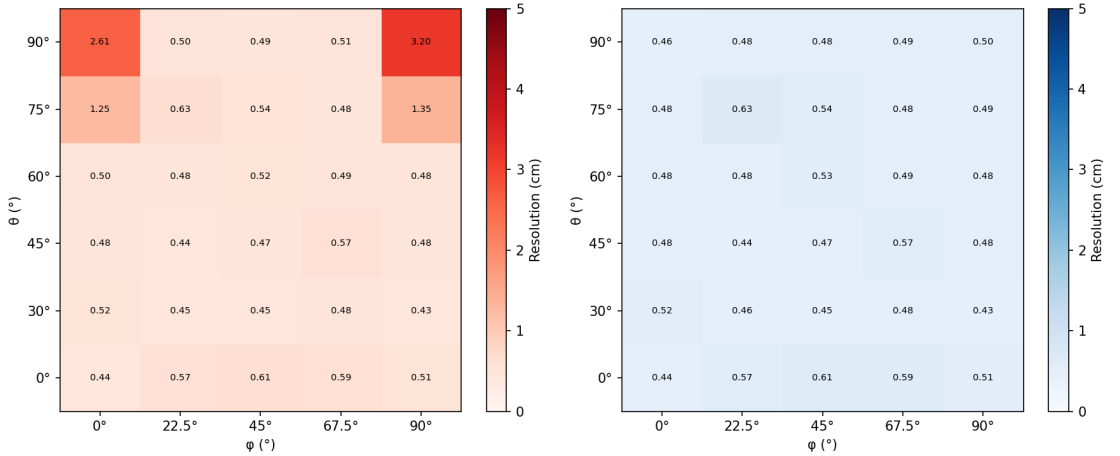


Figure 35: Vertex resolution heatmap at 0.5 cm pitch for $\alpha = 20^\circ$.

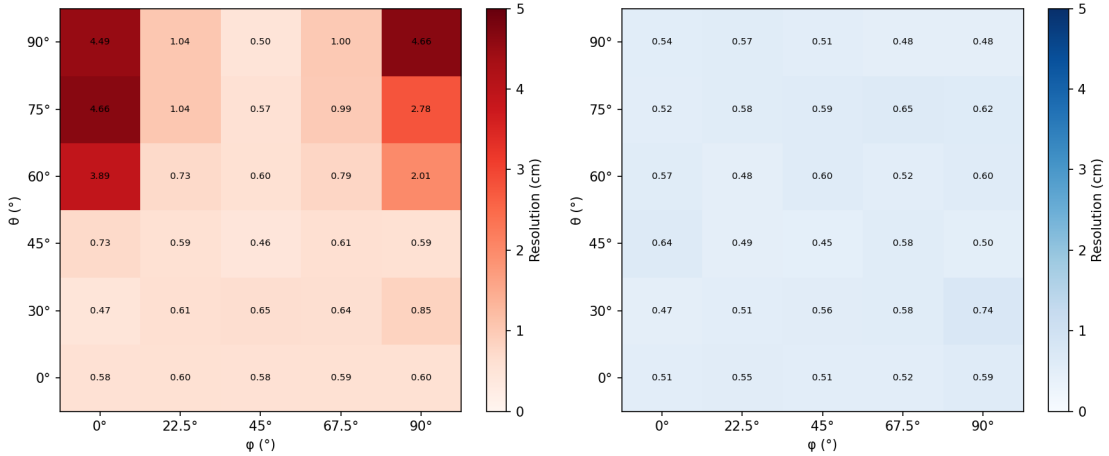


Figure 36: Vertex resolution heatmap at 0.5 cm pitch for $\alpha = 40^\circ$.

A notable feature in Figure 34 is the sharp improvement in resolution (“dip”) at $\theta = 90^\circ, \phi = 45^\circ$ compared to neighboring angles. This effect arises from the interplay between the fine 0.5 cm pitch and the symmetric ghost distribution at 45° . The finer pitch allows the reconstruction algorithm to resolve the conical taper of the shower, which is obscured at 1.0 cm pitch due to coarse voxelization. At exactly 45° , the ghost pattern preserves this taper symmetry, enabling accurate vertex localization. At neighboring angles (e.g., 22.5°), the ghost distribution becomes asymmetric and blocky, disrupting the taper recognition and degrading resolution to levels similar to the 1.0 cm case.

A.7 Energy-Dependent Performance

Figures 37–39 show energy-dependent angular resolution and ghost hits at 0.5 cm pitch for three orientations, using physics-derived track parameters.

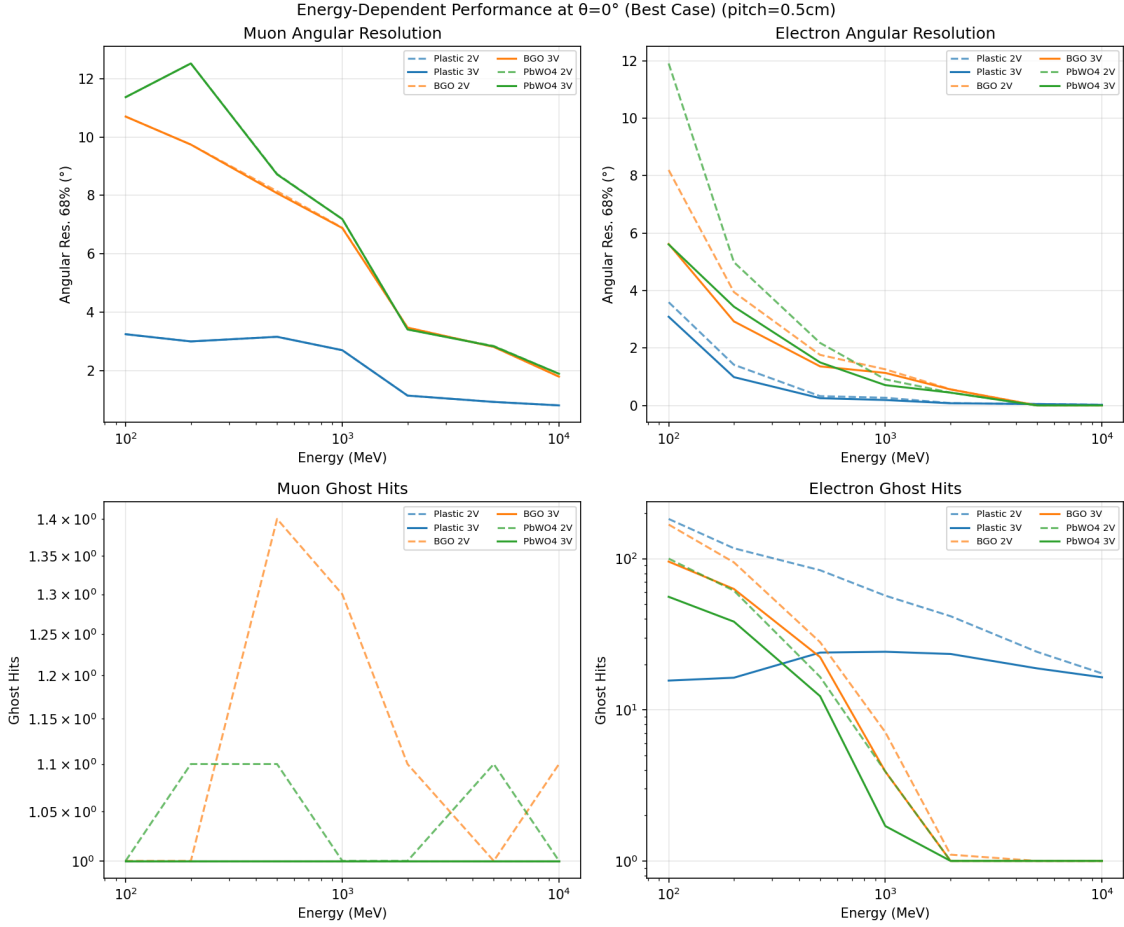


Figure 37: Energy-dependent performance at $\theta = 0^\circ$, pitch = 0.5 cm. Angular resolution improves by approximately 2 \times compared to 1.0 cm pitch across all energies and materials.

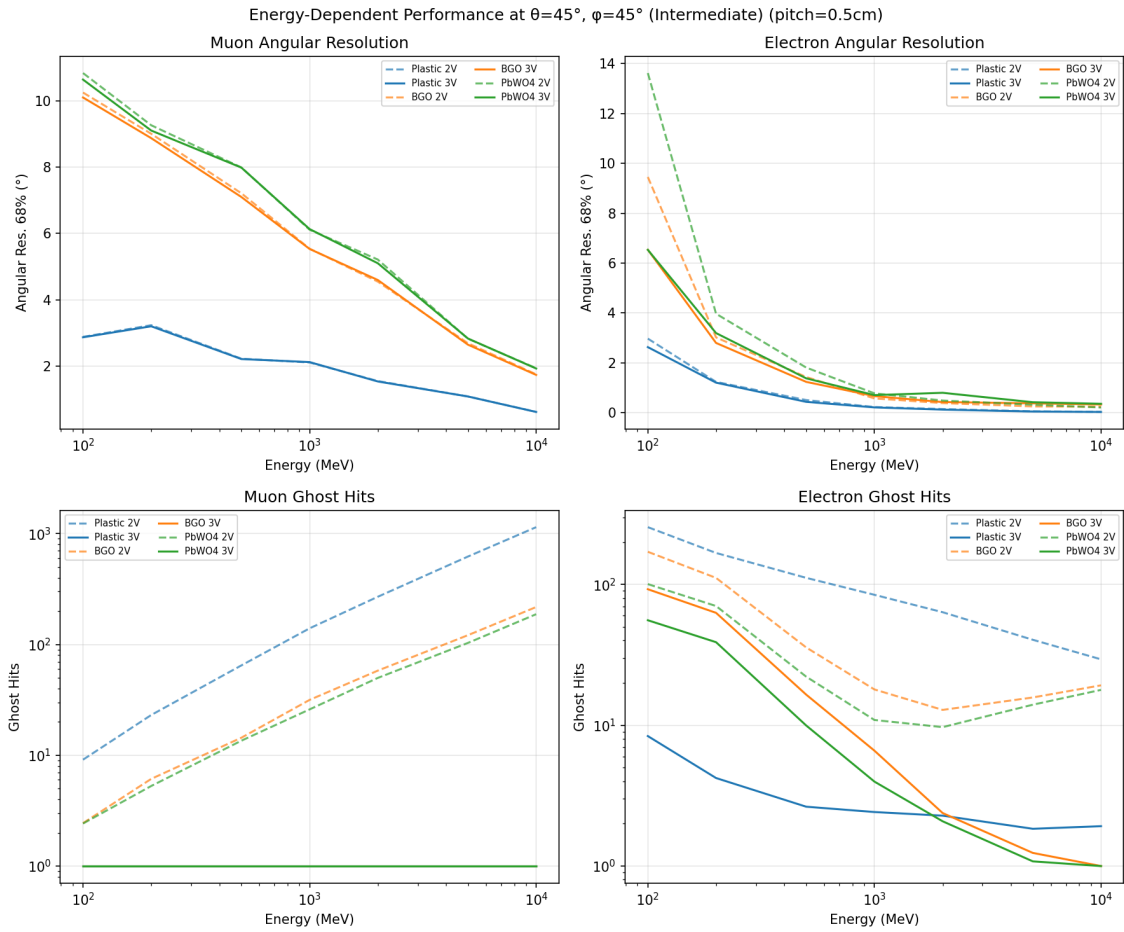


Figure 38: Energy-dependent performance at $\theta = 45^\circ$, $\phi = 45^\circ$, pitch = 0.5 cm.

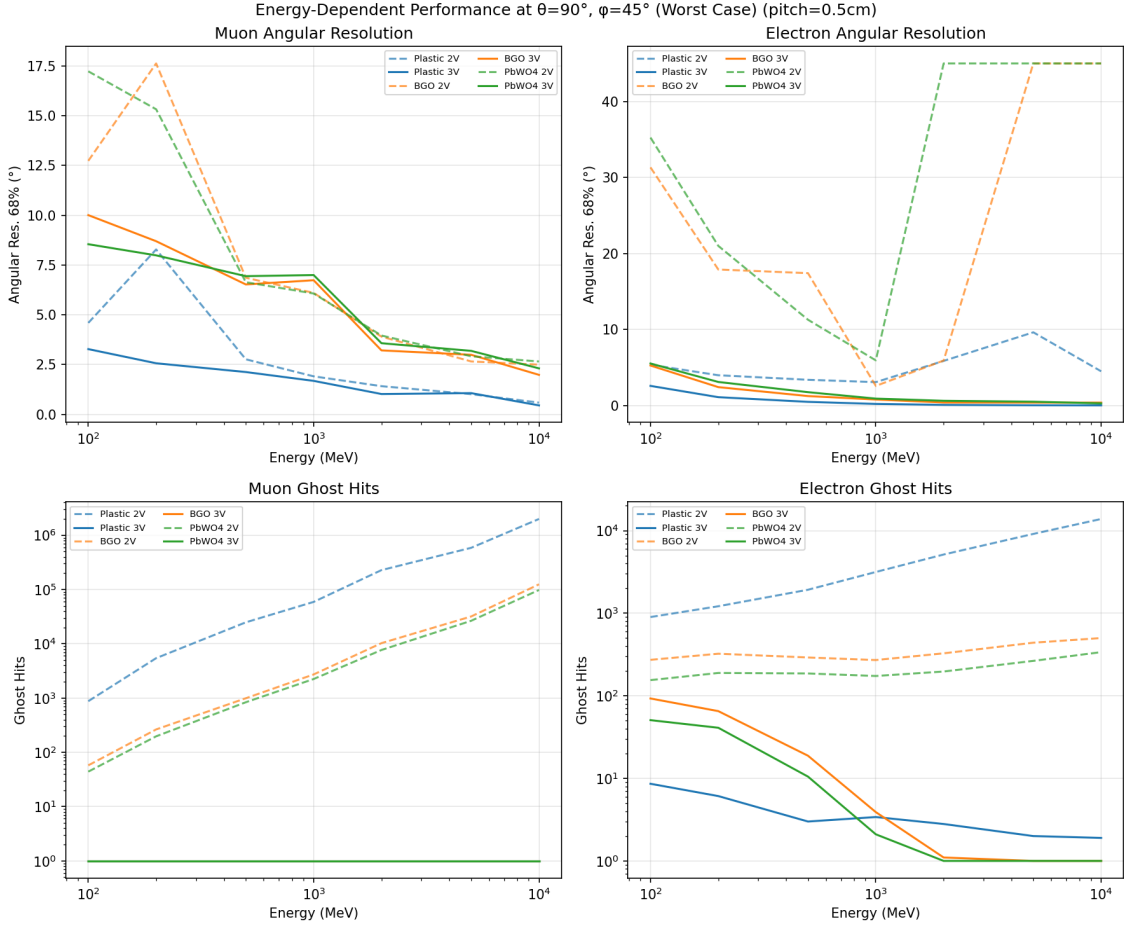


Figure 39: Energy-dependent performance at $\theta = 90^\circ$, $\phi = 45^\circ$, pitch = 0.5 cm. The dramatic 3V advantage at worst-case orientation persists: 2V resolution remains degraded to $\sim 20\text{--}30^\circ$ at low energies, while 3V maintains $<5^\circ$ resolution.

A.8 Summary and Scaling Validation

Table 3 summarizes the resolution scaling from 1.0 cm to 0.5 cm pitch.

Table 3: Resolution scaling from 1.0 cm to 0.5 cm pitch.

Metric	1.0 cm	0.5 cm	Ratio
Angular resolution (3V, $\alpha = 5^\circ$)	$\sim 2^\circ$	$\sim 1^\circ$	2.0
Vertex resolution (single track)	0.29 cm	0.15 cm	1.9
Two-cluster vertex (3V, $\alpha = 5^\circ$)	~ 2 cm	~ 1 cm	2.0
Ghost hit count ($N = 50$, $\alpha = 20^\circ$)	~ 100	~ 100	1.0